Silicon Redistribution, Acid Site Loss and the Formation of a Core-Shell Texture upon Steaming SAPO-34 and their Impact on Catalytic Performance in the Methanol-to-Olefins (MTO) Reaction

Ivalina B. Minova,[1] Nathan S. Barrow,[2] Andrea C. Sauerwein,[2] Aaron B. Naden,[1] David B. Cordes,[1] Alexandra M. Z. Slawin,[1] Stephen Schuyten[3,*] and Paul A. Wright[1,*]

[1] *EaStCHEM School of Chemistry, University of St Andrews, Purdie Building, North Haugh, St Andrews, Fife, KY16 9ST.*

[2] *Johnson Matthey Technology Centre, Blount's Court Road, Sonning Common, Reading. RG4 9NH.*

[3] *Johnson Matthey PLC, 214 Bourne Blvd, Savannah, GA 31408-8501, USA.*

Abstract

SAPO-34 is a commercially-implemented silicoaluminophosphate catalyst for selective high yield production of ethene and propene from methanol, but high temperature regeneration in the presence of steam leads to its deactivation. A comprehensive investigation of the effect of prolonged hydrothermal treatment on the structure and properties of SAPO-34 explains the changes in its catalytic methanol-to-olefins (MTO) performance. Microcrystalline powdered SAPO-34 (*ca.* 3 µm crystals, $Al_{17.1}P_{15.6}Si_{3.3}O_{72}$) and two batches of larger single crystals of SAPO-34 of different Si concentration (20-100 µm; $Al_{17.3}P_{14.7}Si_{4.0}O_{72}$ and $Al_{17.7}P_{12.3}Si_{5.9}O_{72}$) were steamed ($p_{H_2O} = 0.95$ atm) at 873–1023 K for up to 240 h. The acidity (NH_3-TPD), crystallinity (PXRD), framework cation environment (solid-state ^{27}Al, ^{29}Si and ^{31}P MAS NMR) and porosity were followed for all materials; larger crystals were amenable to single crystal X-ray diffraction, FIB-SEM and synchrotron IR microspectroscopy, including *operando* study during methanol and dimethyl ether conversions. Some level of steaming improved the lifetime of all SAPO-34 materials in MTO catalysis without affecting their olefin selectivity, although more severe conditions led to the formation of core-shell structures, microporosity loss and eventually at 1023 K, recrystallization to a dense phase. All these irreversible changes occurred faster in crystals with higher Si contents. The initial increase in catalytic lifetime results from an activated reduction in acid site density ($E_{act} = 146(18)$ kJ mol^{-1}), a result of redistribution of Si within the SAPO framework without porosity loss. *Operando* IR with online product analysis during methanol conversion suggests similar reaction pathways in calcined and steamed crystals, but with greatly reduced methoxy group densities in the latter. The gradual development of optically dark crystal cores upon progressive steaming was shown by FIB-SEM to be due to the formation of regions with meso- and macropores, and these were shown by IR mapping to possess low hydroxyl densities.

Keywords: steamed SAPO-34, methanol-to-olefins, IR spectroscopy and microscopy, FIB SEM

1. Introduction

Methanol-to-Olefins (MTO) and dimethylether-to-olefins (DMTO) conversion have become important worldwide catalytic technologies because of their potential to meet the growing demand for light olefins without relying on petroleum. Existing DMTO technology developed in China is driven by its burgeoning coal-to-olefins industry [1], however, methanol can be derived from renewable feedstocks such as waste biomass, making MTO technology more sustainable. The preferred catalyst used in the commercial MTO process is the silicoaluminophosphate SAPO-34 due to its solid acidity, high selectivity to ethene and propene, hydrothermal stability, and regenerability [2-4]. SAPO-34 adopts the CHA topology type [5] with narrow pore openings (3.8 Å) that allow light olefins (ethene and propene) to leave as products, while aromatic species remain trapped inside the *cha* cavity [6-9].

The acidity in SAPOs required to catalyse the MTO conversion originates from a charge-balancing hydroxyl proton present when Si^{4+} substitutes for P^{5+} in a neutral AlPO framework. The resulting isolated Si species ($Si(OAl)_4$) give Brønsted acidic bridging hydroxyl groups. ‘Silicon islands’, in which there are accumulations of Si in framework positions in the lattice, can also form during synthesis at sufficiently high Si concentrations in the mother liquor [10,11]. Si–O–P linkages are avoided on energetic grounds, which places constraints on the arrangement of Si in an $AlPO_4$ framework [12]. As a result, an island must have $Si(OSi)_4$ species at its centre, while acidity is generated at the edges where Si atoms can be surrounded by 1, 2 or 3 Si next nearest neighbours [12-15]. Some possible Si arrangements are discussed by Vomscheid et al. [11]. The catalytic activity has been shown to be strongly dependent on the Si distribution in SAPO catalysts [16].

After some time on-stream during the MTO/DMTO reaction at 673 – 823 K [3], methyl aromatic species inside the pores fuse together to form large polycyclic aromatic species which cause pore blocking and deactivation [17-20]. This problem is overcome via fluidized bed reactor technology, which allows for the SAPO-34 to be regenerated at high temperatures (823 K – 973 K) in air and recycled [3]. To maintain performance, there is continuous ongoing replacement of irreversibly deactivated catalyst and attritional losses by fresh catalyst, so that the optimal working catalyst has an average age on the order of months. Alternatively, heating in steam can be used for the regeneration, because it permits the controllable partial regeneration of a spent catalyst, and Zhou et al. have shown that this can give enhanced ethylene selectivity [20].

Water vapour may therefore be present at elevated temperature during both reaction and regeneration, and it is therefore important to understand the effect of the hydrothermal treatment of SAPO-34 on its acidic, structural and catalytic properties to optimise its use in the industrial process. Previously, Armburo et al. and Arstad et al. have reported the structural effect of steaming SAPO-34 where magic angle spinning (MAS) solid-state NMR (ssNMR) spectra on isolated samples prepared with enriched ^{29}Si revealed that the environment of silicon atoms changes markedly upon steaming [21,22], with loss of the isolated Si sites, and therefore acidity, in this process. Arstad et al. speculated that the Si is lost from the SAPO-34 to recrystallize to nanoparticles of an all silica zeolite. There are other reports that post-synthetic rearrangement of Si atoms in the framework can occur due to high temperature treatment in steam, which are usually interpreted in terms of the generation of silicon islands, and that these can stabilise nanoparticles of SAPO-34 [23-25]. Theoretical studies of aluminosilicate island formation have been used to simulate the effect of steam on the SAPO-34 structure where a Si atom leaves the structure by hydrolysis and a P atom fills the vacancy [26]. According to this mechanism, to maintain the framework structure, Si might eventually migrate to a vacancy left adjacent to the aluminosilicate islands, extending them, although Al migration would also be required. However, the ssNMR evidence in the literature for growth of aluminosilicate islands by desilication remains inconclusive. Other changes that were observed by Aramburo et al. and Arstad et al. during steaming at 973 K include loss of micropore volume, contraction in the unit cell, development of a small additional peak in the ^{31}P MAS ssNMR and changes in the Brønsted acidity [21,22]. However, only one steaming condition was reported in each paper at 973 K making it hard to correlate the changes in properties and structure.

Here we present a comprehensive investigation on the changes of the crystallinity, porosity and acidity that result from the exposure of a commercial microcrystalline SAPO-34 to industrially-relevant hydrothermal treatment, or 'steaming' [3,20]. This enables us to relate measured changes in catalytic performance of the steamed materials in MTO to the modifications of their structure. To glean additional insight into the structural changes occurring during steaming, we have also prepared two batches of SAPO-34 crystals, with different Si contents, comprising 'large' single crystals (>10 μm) and carried out steaming, characterisation and measurements of their catalytic activity. Although these larger crystal samples are poor catalysts because they deactivate quickly, we find that their structural and textural response to steaming and the resulting effects on their catalytic lifetime are comparable to those of the microcrystalline materials. Crucially, their large size makes them more amenable to FIB-SEM, SCXRD and synchrotron IR microspectroscopy, which help elucidate the mechanisms by which steaming initially enhances and then reduces the catalytic lifetime of this technologically-relevant catalyst.

2 Experimental

2.1 Synthesis and Characterisation of Materials

Sample LC-SAPO-34-A was prepared via a modified literature procedure with reduced SiO_2 content in the synthesis gel [27]. H_3PO_4, 85% (6.12 g, 53 mmol), $Al(OH)_3$ (4.80 g, 50 mmol), morpholine (4.56 g, 52 mmol) were added to deionised water (35.18 g, 2.00 mol) and fumed silica (0.602 g, 10 mmol) was slowly added. The gel (composition 1.0 $Al(OH)_3$: 1.06 H_3PO_4 : 0.2 SiO_2 : 40 H_2O : 1.05 morpholine) was stirred at 313 K for 16 h before being sealed in a Teflon lined autoclave (125 mL, Parr) and heated at 463 K for 5 d under static conditions. The solid was recovered by vacuum filtration, washed with deionised water and dried overnight at 373 K. Prior to spectroscopic measurements, the crystals were freshly calcined at 823 K (2 K min^{-1}) in air for 14 h.

For sample LC-SAPO-34-B H_3PO_4, 85% (4.04 g, 35 mmol), $Al(OH)_3$ (4.80 g, 50 mmol), morpholine (3.05 g, 35 mmol) were combined with deionised water (35.49 g, 2.00 mol) and fumed silica (0.903 g, 15 mmol) was slowly added following a modified literature procedure for high Si

SAPOs [28-30]. The gel composition (1.0 $Al(OH)_3$: 0.7 H_3PO_4 : 0.3 SiO_2 : 40 H_2O : 0.7 morpholine) was stirred at room temperature for 2 h before being sealed in a Teflon lined autoclave (125 mL, Parr) and heated at 463 K for 5 d under static conditions. The solid product was recovered by vacuum filtration, washed with deionised water and dried overnight at 373 K. Prior to spectroscopic measurements, the crystals were calcined at 823 K (2 K min^{-1}) in air for 14 h to give the proton form.

A microcrystalline SAPO-34 in the protonic form and binder free, was obtained from Zeolyst (reference number CP7129 and labelled as such hereafter).

Powder X-ray Diffraction (PXRD) patterns were obtained in reflection mode at room temperature with primary monochromation (Cu $K_{\alpha 1}$, λ = 1.54051 Å), on Bruker D2 or D8 instruments. Prior to analysis samples were pressed into a flat disk. Phase identification of samples was accomplished by direct comparison of the observed patterns with that for SAPO(CHA) calculated using the SAPO(CHA) structure from the *IZA* database [5] via the CrystalDiffract software [31].

For structural analysis and refinement of dehydrated calcined materials, samples were loaded in 0.7 mm diameter quartz glass capillaries and dehydrated at 573 K under a vacuum of 10^{-5} mbar for 5 h before being sealed. X-ray powder diffractograms were then collected in Debye-Scherrer mode at room temperature over a 2θ range 5–70° (step size 0.1°, time step 80 s, 40 kV, 35 mA) on a Stoe STAD I/P diffractometer with a primary monochromator and PSD detector using Cu $K_{\alpha 1}$ X-ray radiation (λ = 1.54056 Å). Rietveld refinement of calcined and calcined and steamed SAPO-34 materials was carried out using the GSAS suite of programs via the EXPGUI graphical interface [32,33]. The structure of SAPO-34 was refined in the *R*-3 space group, using the models derived from the single crystal analyses (see below) as the starting point. The instrumental background was fitted automatically by using a Chebyschev function. The peak profiles were modelled using a Pseudo-Voigt function (type 2). The framework Al-O, P,Si-O, O-O(Al), and O-O(P,Si) distances were soft constrained to 1.72 Å (σ = 0.020 Å), 1.53 Å (σ = 0.020 Å), 2.82 Å (σ = 0.005 Å), and 2.48 Å (σ = 0.005 Å), respectively.

Selected samples were analysed by Single-Crystal X-ray Diffraction (SCXRD). SCXRD data were collected at 173 K using a Rigaku MM-007HF High Brilliance Microfocus RA generator/confocal optics with XtaLAB P100 diffractometer [Cu K_α (λ = 1.54187 Å)]. Intensity data were collected using 0.5° ω- or φ-steps accumulating area detector images spanning at least a hemisphere of reciprocal space. Data for all compounds analysed were collected using CrystalClear [34] and processed (including correction for Lorentz, polarization and absorption) using CrysAlisPro [35]. Structures were solved by dual-space methods (SHELXT) [36] and refined by full-matrix least-squares against F^2 (SHELXL-2018/3) [37]. The structures were refined in the space group *R*-3 (which was found to be more likely than *R*3). All atoms were refined anisotropically. Both structures showed pseudo-merohedral twinning, with a twin law of [-1 0 0 1 1 0 0 0 -1] and refined twin fractions of 0.09 and 0.23, respectively. In both structures P and Si were constrained to share the same atomic sites, with occupancies fixed at a P:Si ratio of 7:2. Both structures structure showed high proportions of void space (LC-SAPO-34-B: 1082 $Å^3$, LC-SAPO-34-B-973-44: 1068 $Å^3$) and the SQUEEZE [38] routine implemented in PLATON [39] was used to remove the contribution to the diffraction pattern of the unordered electron density in the void spaces. All calculations except SQUEEZE were performed using the CrystalStructure interface [40]. Selected crystallographic data are presented in Table S1. Deposition numbers 2039327 and 2039328 (calcined, LC-SAPO-34-B; and steamed, LC-SAPO-34-B-973-44, respectively) contain the supplementary crystallographic data for this paper. These data are provided free of charge by the joint Cambridge Crystallographic Data Centre and Fachinformationszentrum Karlsruhe Access Structures service www.ccdc.cam.ac.uk/structures.

Thermogravimetric analysis (TGA) was conducted on a TA Instruments Discovery TGA in the temperature range 298–1173 K using ~15 mg of sample. To analyse the loss of water, the calcined samples were heated in flowing nitrogen at a heating rate of 20 K min^{-1}. When samples contained coke forming hydrocarbons, they were analyzed using a two-step program first flowing nitrogen between 298–523 K, then switching to flowing air from 523–1173 K, both at a heating rate of 20 K min^{-1}. TGA measured water loss on the pre-equilibrated samples was used to correct for moisture content on all analyses. The weight% of the elements present were determined by X-ray fluorescence (XRF) spectroscopy.

Scanning Electron Microscopy (SEM) and Focused Ion Beam (FIB) milling were performed on a FEI Scios dual beam instrument equipped with an EDAX Octane Plus energy dispersive X-ray spectroscopy (EDX) detector. Samples were prepared by dispersion in ethanol and drop cast on single crystal Si wafer purchased from Labtech International Ltd. SEM imaging was performed at an acceleration voltage of 3 kV following identification of appropriate crystals via light microscopy. Prior to cross-sectioning, protective Pt caps were deposited with the electron beam (at 5 kV) to a thickness of ~ 0.25 μm followed by the ion beam (~ 1 μm at 30 kV). FIB milling was performed at an acceleration voltage of 30 kV with successively decreasing beam currents with nominal values of 15, 7, 5, 3 and 1 nA. EDX spectra were acquired with an electron beam acceleration voltage of 5 kV.

Temperature-programmed desorption of ammonia (NH_3-TPD) was performed on a Micrometrics AutoChem II Chemisorption analyzer. For each experiment ~ 300 mg of SAPO-34 crystals were loaded into the U-shaped quartz tube supported on a quartz wool plug, which was placed inside the instrument furnace. The sample was dehydrated by heating to 923 K (15 K min^{-1}) under He. Then, the temperature was cooled to 373 K (35 K min^{-1}). After cooling to 373 K, the gas flow was switched to 5,000 ppm NH_3 (45 cm^3 min^{-1}) in He (30 cm^3 min^{-1}) for 90 min. The reactor chamber was then flushed with He for 30 min at 373 K (25 K min^{-1}) to remove any excess NH_3 before monitoring desorption. Then the temperature was cooled to 333 K (5 K min^{-1}). Ammonia was desorbed with a gradual temperature increase from 333 K to 923 K (10 K min^{-1}). The catalyst was held at 923 K for 15 min to ensure all the ammonia was desorbed. The TPD profiles show two peaks, a low temperature and high temperature peak, with the high temperature peak ascribed to the loss of ammonia from the Brønsted acid site (BAS) [41]. The TCD NH_3 signal was calibrated using ammonia in helium (certified 5000 ppm) and measuring the TCD signal with ammonia flows adjusted to concentrations of between 0 and 5000 ppm to generate a calibration line. The total amount of ammonia desorbed during the heating ramp was calculated from the integrated intensity under the TCD signal by drawing a flat baseline and separating the two overlapping peaks at the minimum.

Nitrogen adsorption was carried out primarily on a Micrometrics 3Flex equipped with 0.1, 10, and 1000 torr transducers on each port. Samples underwent a 2-stage degas procedure: first ex-situ at 673 K for 480 min on Micromeritics high vacuum capable Smart VacPrep with nitrogen backfill, then in situ on the 3Flex under high vacuum at 623 K for 240 min. Nitrogen dosing below p/p_0 = 0.01 was performed with a fixed increment of 4 cm^3 g^{-1} followed by pressure increment dosing of 0.01 to 0.995 p/p_0. The instrument limit of detection (< 2%) was confirmed by performing repeats using a reference sample. For some confirmatory experiments a Micromeritics ASAR 2020 volumetric analyser was used on the Zeolyst samples steamed at 923 K.

Magic angle spinning (MAS) solid-state nuclear magnetic resonance (ssNMR) spectra were acquired at a static magnetic field strength of either 9.4 T ($\nu_0(^1H)$ = 400 MHz) for ^{29}Si or 14.1T ($\nu_0(^1H)$ = 600 MHz) for ^{27}Al and ^{31}P. For ^{27}Al, the probe was tuned to 156.40 MHz and referenced to YAG at 0.0 ppm. For ^{29}Si, the probe was tuned to 79.51 MHz and referenced to kaolinite at −91.2 ppm. For ^{31}P, the probe was tuned to 242.98 MHz and referenced to ADP at 0.9 ppm. Powdered samples were dried at 383 K before being packed into zirconia MAS rotors with Kel-F caps. The rotors were spun using room-temperature purified compressed air with MAS rates of 14,000 Hz, 4000 Hz or 10,000 Hz for ^{27}Al, ^{29}Si and ^{31}P, respectively. All spectral intensities have been normalised based on the experimental parameters such as sample mass and number of scans so that quantitative spectra can be compared.

2.2 Hydrothermal treatment and Catalytic studies

For hydrothermal treatment, or steaming, each sample (up to four samples at a time) was mounted inside a horizontal quartz tube at 473 K. The temperature was then ramped (5 K min^{-1}) to the desired steaming temperature before water was introduced into the system. A peristaltic pump delivered water (0.507 g min^{-1}) in a constant flow of nitrogen (33 cm^3 min^{-1}, SCCM). When evaporated this gives steam at 19× the molar flow rate of nitrogen (the gas flow then contains 95% steam). Steam (95%) was delivered for a fixed time (between 5–256 h); water was then switched off and the temperature was reduced to 473 K before removing the samples. Each sample was left to fully hydrate overnight inside a chamber with fixed 50% relative humidity at room temperature prior to further analysis. The steaming protocol was developed using the commercial CP7129 sample, starting with steaming at 923 K (20-206 h) and expanding it to lower and higher temperatures (Table 1).

Table 1. Duration span of steaming for each sample in the 823-1023 K range.

Temperature	**CP7129**	**LC-SAPO-34-A**	**LC-SAPO-34-B**
873 K	20–282 h	-	-
923 K	20–206 h	20–206 h	20–256 h
973 K	20–137 h	20–44 h	20–72 h
1023 K	5–113 h	5–20 h	5–20 h

For catalytic measurements, CP7129 samples were pressed using a 31 mm die (10 tons, 10 min) then crushed and sieved between 150-300 μm mesh. The pellets obtained were weighed (0.33 g) and mixed with SiC (2.5 g, 120 grit). For the two large LC-SAPO-34 crystals (0.33 g) samples were mixed directly with SiC diluent (2.5 g, 46 grit) without prior crushing or pressing. The sample was loaded inside the stainless steel microreactor (9 mm, downward flow) using quartz wool plugs and mounted inside a furnace. Catalytic testing was typically performed at 723 K and mass balance was 100 ± 5% using the known input flow rates of methanol and Ar/N_2 compared to the detected hydrocarbons.

For the CP7129 materials, 95% methanol and 5% water were delivered using a Gilson HPLC pump (flow rate 0.0371 mL min^{-1}) to a vaporizer which was purged with an MFC controlled 15 SCCM Ar/N_2 gas blend, giving a WHSV(CH_3OH) of 7 h^{-1}. On the two large SAPO-34 crystals, a diluted 40% methanol 60% water mixture was used WHSV(CH_3OH) = 3 h^{-1} to slow down the coke deactivation, as it has been shown that using a water-methanol mixture prolongs the induction period in the MTO conversion [42]. The methanol feedstock was sonicated prior to loading to remove dissolved gas. During the reaction, the gas phase products was analysed by a highly customized on-line Agilent 7890B GC equipped with 6 columns (including a RT-Q-BOND capillary column (30 m × 0.32 mm) downstream from a CP-Sil 5 CB Agilent column (10 m × 0.32 mm) and 2 FID (573 K) and a TCD (523 K) detectors for analysis of hydrocarbons C_1 to C_6, oxygenate compounds, and permanent gases respectively. Weight hourly space velocity (WHSV) was calculated as the weight of feed flowing per unit weight of the catalyst per hour. Conversion and its related terms yield, and selectivity are defined as percentage of reactant converted to products (between zero and 100%).

For in situ catalysis / IR microspectroscopy, a fresh batch of calcined SAPO-34 crystals was used for each IR measurement. The crystals (< 3 mg) were loaded onto a CaF_2 window, which was placed on the heated sample stage of an environmental Linkam FTIR600 cell (with an internal volume of 50 mL) mounted on a Hyperion 3000 IR (Bruker) microscope coupled to a Vertex 80V FTIR at MIRIAM beamline B22 of the Diamond Light Source synchrotron [43]. Gas flow of ultra-dry nitrogen (100 mL min^{-1}) was delivered to the Linkam cell by mass-flow controller and pulses of spectroscopic grade (≥ 99.8%) methanol, were injected into the gas stream via microsyringe. The outlet from the cell was directed to an on-line quadrupole mass spectrometer (Hiden) for analysis of gas phase products. Repeated IR spectra were measured during the injection of methanol into fresh SAPO-34 crystals at 523–673 K under ambient pressure, or in flowing dimethyl ether (5 mL min^{-1}) both diluted in flowing nitrogen (100 mL min^{-1}). A 2 s time resolution was achieved by averaging 16 single-sided interferograms at 4 cm^{-1} for each spectrum For IR mapping experiments, an aperture of 10 × 10 μm^{2} and an oversampling of 5 μm were utilized. Background measurements were performed with a spectral resolution of 4 cm^{-1} and 64 scans per spectrum.

3. Results

3.1 Synthesis and characterisation

Large crystal batches of SAPO-34 (LC-SAPO-34 samples A and B) were prepared under hydrothermal conditions using morpholine as the structure directing agent and fumed silica (0.007 µm) as the silica source while a microcrystalline SAPO-34 in the protonic form was obtained from Zeolyst (CP7129).

The PXRD patterns and SEM micrographs of the protonic forms of the three SAPO-34 samples used in this study are shown in Figure 1. Microcrystalline CP7129 consists of crystals below 3 µm in size, while the two LC-SAPO-34 samples consist of larger crystals with sizes in the range 20-100 µm. The diffraction pattern of CP7129 shows some peak broadening, which is attributed to small crystallite size. Small amounts of berlinite crystals (main peak at about ~21° 2θ) were present as an impurity in the lower silica large crystal batch, which appear as dark crystals of different shape under the optical microscope and so are easy to differentiate.

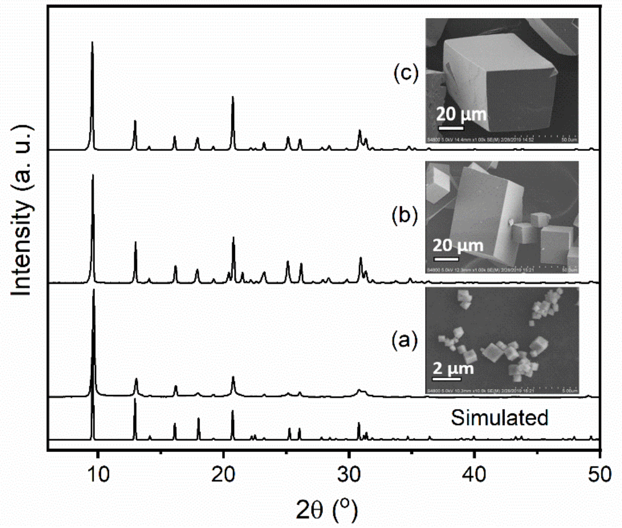

Figure 1. Simulated PXRD pattern of SAPO-34 (using SAPO(CHA) from [5], calculated via CrystalDiffract software [31]) compared to the PXRD pattern of the three calcined crystals used in this steaming study: Zeolyst CP7129 (image a) LC-SAPO-34-A (image b) and LC-SAPO-34-B (image c).

All calcined samples are highly porous; details of their specific composition (by XRF), acidity (by NH_3-TPD) and BET surface area (N_2 adsorption) are given in Table 2. CP7129 and LC-SAPO-34-A have a comparable composition (9.2 mol% and 11.1 mol% of Si within tetrahedral cation sites, respectively), while LC-SAPO-34-B has a higher Si content (16.4 mol%), reflecting the higher Si content used in the synthesis gel.

Table 2. Summary of characterisation parameters for the samples in this steaming study.

Crystal name	**CP7129**	**LC-SAPO-34-A**	**LC-SAPO-34-B**
Crystal size (SEM)	<3 µm	20–100 µm	20–100 µm
Composition (XRF)	$Al_{17.1}P_{15.6}Si_{3.3}O_{72}$	$Al_{17.3}P_{14.7}Si_{4.0}O_{72}$	$Al_{17.7}P_{12.3}Si_{5.9}O_{72}$
HTP (NH_3-TPD) Si atoms (XRF)	1.4 mmol g^{-1} 1.5 mmol g^{-1}	1.2 mmol g^{-1} 1.8 mmol g^{-1}	1.7 mmol g^{-1} 2.8 mmol g^{-1}
Si atoms per CHA cage	1.1	1.3	2.0
t-plot pore volume (N_2) & BET surface area	0.24 cm^3 g^{-1} ~ 690 m^2 g^{-1}	0.24 cm^3 g^{-1} ~ 680 m^2 g^{-1}	0.25 cm^3 g^{-1} ~ 700 m^2 g^{-1}

Additionally, LC-SAPO-34-A and LC-SAPO-34-B samples were embedded in resin and sliced then polished so that the elemental compositions of the resulting cross sections mapped by EDX (Figure

S1, in the SI). These crystals exhibit a homogeneous distribution of Si, P and Al, unlike those reported by Liu et al. [44] for which a non-uniform distribution of silicon was measured, increasing from the core to the surface.

The Si distribution in the as-made and calcined materials was characterised by ^{29}Si MAS ssNMR spectroscopy and compared to samples in the literature (Figure 2). The ^{29}Si ssNMR spectra of the large crystal samples show some broadening, particularly after calcination. All spectra in the materials of this study are dominated by $Si(OAl)_4$ at −94.3 ppm and $Si(OAl)_3(OSi)$ resonances at −100 ppm, although there is evidence of minor amounts of $Si(OSi)_4$ species, which would indicate some silicon islands, particularly in LC-SAPO-34-B. This explains why the acid site concentration in the large crystal samples are lower than the amount of included Si, as also suggested by Vomscheid et al. [11], who observed an upper limit to the overall framework charge in SAPO-34.

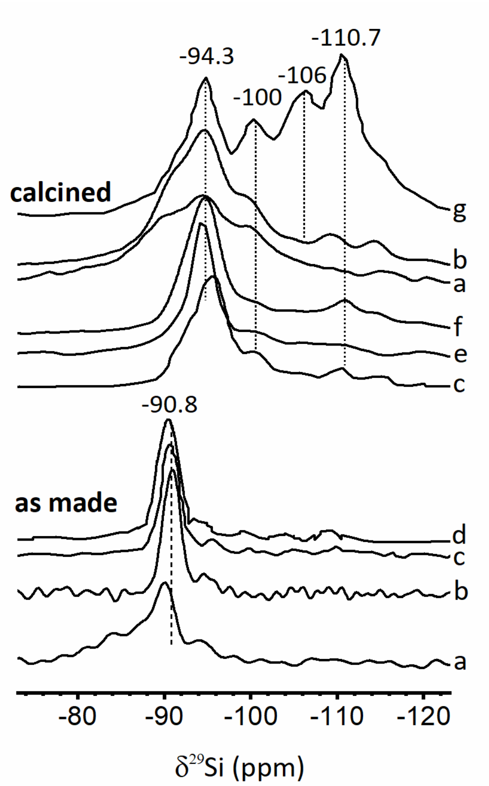

Figure 2. ^{29}Si MAS-ssNMR spectra of the three SAPO-34 crystals (not ground) used in this steaming study and comparison with examples from the literature. (a) LC-SAPO-34-A; (b) LC-SAPO-34-B; (c) Briend et al. [45]; (d) Tan et al. [10]; (e) Arstad et al. [22]; (f) SAPO-34 CP7129 and (g) Li et al [25].

3.2 Effect of steaming on the crystallinity, acidity and Si distribution

CP7129 samples were initially steamed at 923 K, a typical operating temperature for the MTO catalyst regenerator [46]. The sample remains highly crystalline and nitrogen adsorption isotherms reveal no loss in micropore volume even after steaming for 206 h (Figure 3). Nevertheless, according to NH_3-TPD, more than 40% of the Brønsted acid sites (BAS) are lost after steaming for 206 h. The Brønsted acidity is mostly associated with the isolated silicon environment $Si(OAl)_4$ at –94.5 ppm. With progressive steaming a reduction in the signal from this isolated silicon is seen, consistent with the observed reduction in acidity measured by NH_3-TPD. The Si redistribution after steaming gives ^{29}Si resonances at –101, –107, –111, –115 and –121 ppm, which increase in intensity with increasing severity of steaming and correspond to silicon islands.

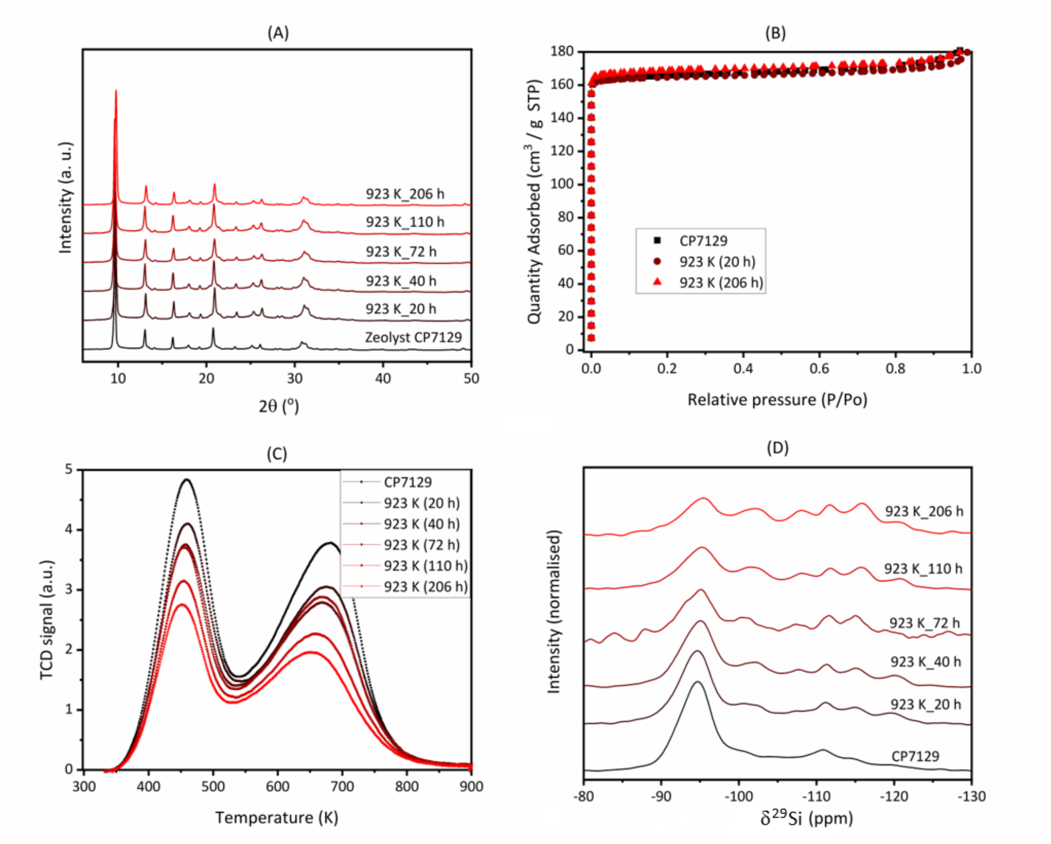

Figure 3. SAPO-34 (CP7129) steamed at 923 K between 20 h and 206 h. (A) PXRD patterns; (B) N_2 isotherms (77 K); (C) NH_3-TPD profiles normalised against mass and (D) ^{29}Si MAS-ssNMR spectra normalized by mass and number of scans.

At the lower temperature of steaming, 873 K, there is relatively little decrease in the Brønsted acidity and no loss in crystallinity or micropore volume (Figure S2). There is a similar change in the ^{29}Si spectrum, as the Si(OSi)$_4$ peak decreases and the development of the silicon island resonances at −101, −107, −111, −115 and −121 ppm, while apparent, is less marked at 873 K.

At the higher steaming temperature of 973 K (Figure 4) the micropore volume suddenly drops after 116 h of steaming and some evidence for the growth of small amounts of a new crystalline phase is observed in the PXRD patterns (small peaks observed at 2θ values at 20.4, 21.5, 23.0, 35.7°). The ^{29}Si profile in the MAS-ssNMR spectrum at this time (973 K_116 h) develops to reveal the same Si environments seen for the lower temperatures but here the changes in the ^{29}Si ssNMR and the reduction in Brønsted acidity occur much more rapidly (Figure 5).

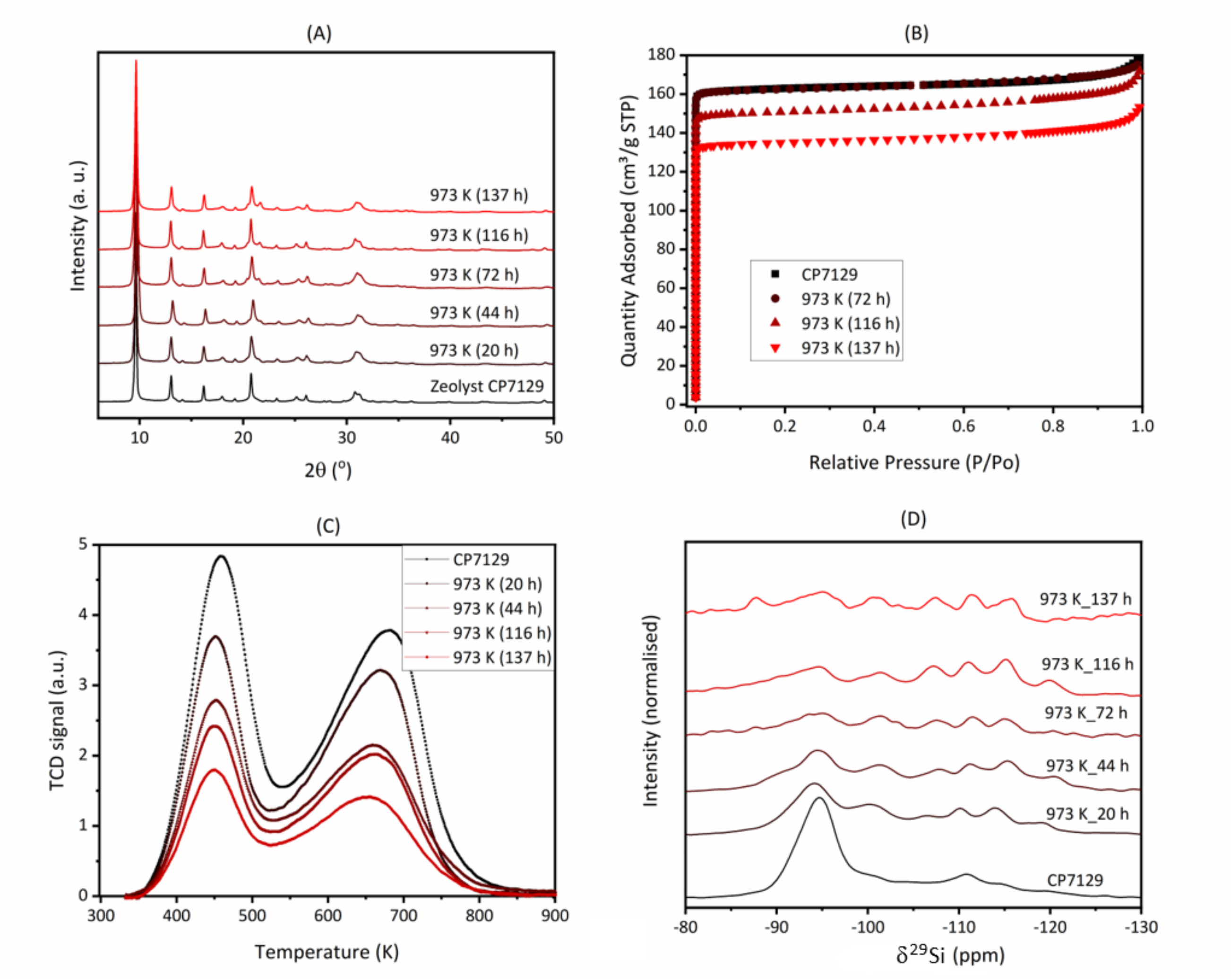

Figure 4. SAPO-34 CP7129 steamed at 973 K between 20 h and 137 h. (A) PXRD patterns; (B) N_2 isotherms (77 K); (C) NH_3-TPD profiles normalised against mass and (D) ^{29}Si MAS-ssNMR spectra normalized by mass and number of scans.

Finally, steaming at 1023 K for longer than 10 h caused a rapid decline in micropore volume until the sample was no longer porous to nitrogen after 113 h (Figure S3). X-ray diffraction revealed structural transformation to a dense SAPO phase (2θ values at 20.4, 21.5, 23.0, 35.7°). When the complete transformation to this dense phase is achieved (1023 K_113 h), a single broad ^{29}Si resonance at −116 ppm is observed, in strong contrast to the multiple well-defined peaks seen at lower steaming temperatures (Figure 5). This is associated with a loss in microporosity, as would be expected (Figure S3).

Figure 5 shows that the observed ^{29}Si resonances for the steamed samples do not match the resonances for Si(OAl,OSi)$_4$ islands of SAPO-34 prepared by direct synthesis and then calcined – that is, steaming causes silicon redistribution within the SAPO. Our series of samples show gradual increases in well-defined resonances at −101, −107, −111, −115 and −121 ppm, similar to that reported by Arstad et al. [22] for individual samples.

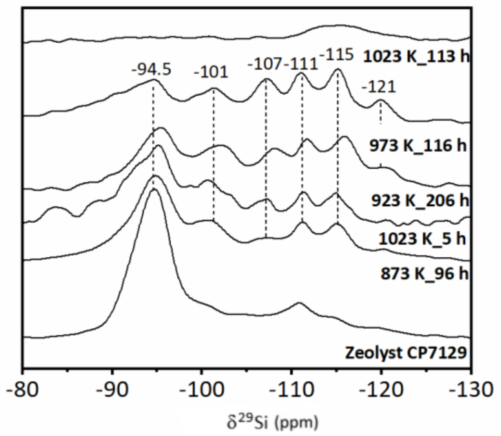

Figure 5. ^{29}Si MAS-ssNMR spectra of steamed SAPO-34 samples showing that different temperatures and times of steaming result in the same Si distribution; i.e. redistribution is a kinetic effect.

In Figure S4 the ^{29}Si MAS-ssNMR of steamed CP7129 (973 K_116 h) is compared with that of Arstad et al. (973 K_168 h): the extra ^{29}Si resonances at −94.5, −101, −107, −111, −115 and −121 ppm are much better developed in the former. Notably, the ^{1}H-^{29}Si CP analysis of the steamed (973 K_168 h) sample showed [22] only the ^{29}Si species at −94.5 and −100 ppm were in proximity to H, indicating the rest of the upfield ^{29}Si species do not have protons associated with them.

Analysis of the NH$_3$-TPD measurements confirms that the loss of acidity is closely related to the decrease in the Si(OAl)$_4$ resonance and development of the new peaks. Similar ^{29}Si spectra are observed for samples subject to short duration steaming at 1073 K and prolonged steaming at 923 K, indicating the process is kinetically limited (Figure 5). A full kinetic analysis was performed using the acid site density measured by NH_3-TPD, because these data were more quantitative. The decrease in acid site concentration appears to follow first order kinetics, so that *ln*[BAS] decreases linearly with time at all temperatures (Figure 6). Using this model it is possible to derive first order rate constants at the four temperatures (Table 3), and thereby the activation energy, via an Arrhenius plot, which is 146(18) kJ mol^{-1}.

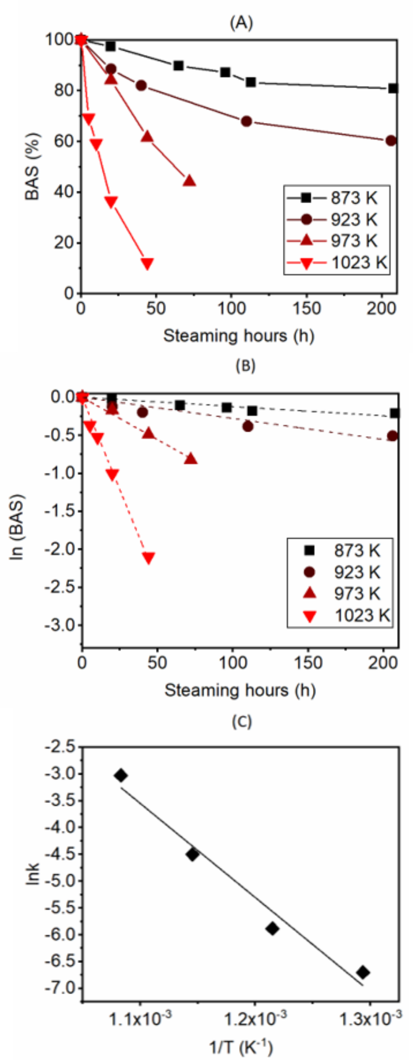

Figure 6. (A) BAS expressed as percentage relative to the calcined (non-steamed) SAPO-34 (CP7129); (B) corresponding logarithmic plots, assuming first order kinetics; (C) Arrhenius plot of the first order rate constants for BAS removal from the SAPO-34 (CP7129).

Table 3. Rate constants for the SAPO-34 CP7129 and the two LC-SAPO-34 samples, assuming the data fits a first-order process. See Figure S1 for analysis on sample LC-SAPO-34-A.

Rate constant / h^{-1}	**CP7129**	**LC-SAPO-34-A**	**LC-SAPO-34-B**
k_{873}	0.00123 ± 0.0001	-	-
k_{923}	0.00278 ± 0.0003	0.0066 ± 0.0011	0.0078 ± 0.0002
k_{973}	0.0111 ± 0.0004	0.015 ± 0.007	0.047 ± 0.007
k_{1023}	0.04854 ± 0.0014	0.056 ± 004	-
E_a (kJ mol^{-1})	146 ± 18	135 ± 26	-

Steamed samples were also analysed by ^{31}P and ^{27}Al MAS-ssNMR (Figures 7, S6, S7 and S8) and all show the same trends. Figure 7 shows the expected $P(OAl)_4$ signal [22] at −30 ppm for CP7129 and, after steaming at 973 K, an additional weak peak at −34.4 ppm that increases to ~ 3% of the total P intensity. No significant changes occur in the ^{27}Al MAS-ssNMR after steaming, other than some sharpening of the main tetrahedral resonance at ca. 36 ppm [47].

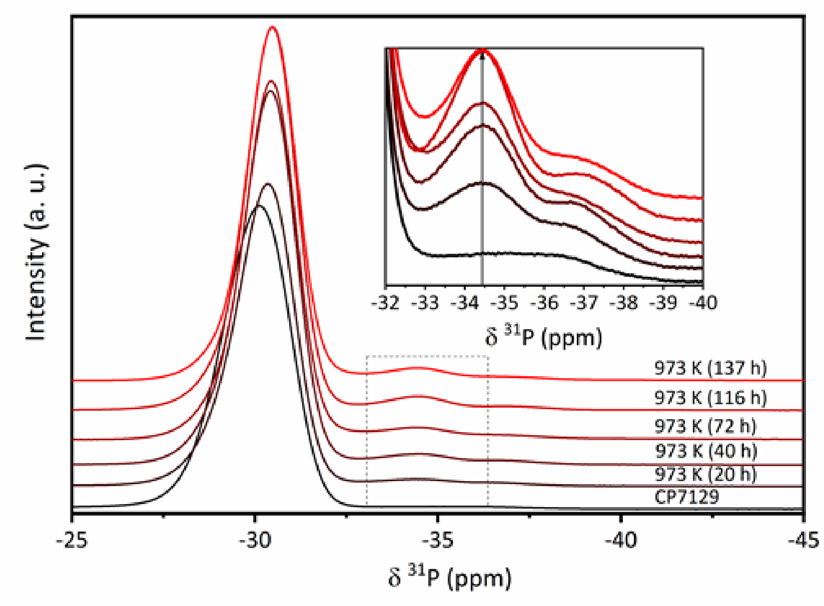

Figure 7. ^{31}P MAS-ssNMR spectra of CP7129 steamed at 973 K for increasing durations from 20 to 137 h. The expansion highlights the growth of the ^{31}P peak at -34.4 ppm.

For comparison, the two batches of large crystals were steamed using the same protocol as for the microcrystalline powder. Characterisation is shown in Figure 8 for SAPO-34-A and Figure 9 for SAPO-34-B, respectively. XRF analysis confirmed the presence of all SAPO elements Al, P and Si, indicating that the bulk Si has remained in the sample and there is no loss of Si from the crystals during steaming (also confirmed by EDX, shown in Figure S9). The structural response of both sets of large crystals to steaming follows a similar trend to that observed for the microcrystalline material, with loss in BAS and redistribution of silica occurring rapidly, followed by loss of microporosity and, later, crystallinity.

The changes in Brønsted acidity and micropore volume are much more marked for the high Si sample (LC-SAPO-34-B) and are consistent with the major changes seen in its ^{29}Si MAS-ssNMR spectra, e.g. LC-SAPO-34-B at 44 h, 973 K, Figure 9. Analysis of the kinetics of loss of BAS in the single crystals in terms of a first order process gives the rate constants of Table 3. The changes in the ^{29}Si MAS-ssNMR spectrum for the CP7129 and the large crystal sample B, displayed as difference plots, are compared in FigureS10. The new peaks are more intense in LC-SAPO-34-B but occur at the same chemical shifts.

PXRD patterns (in panel (A) of Figures 8 and 9) indicate both samples (large crystals A and B), treated at 973 K for less than 50 h, remain highly crystalline. However, N_2 77 K adsorption isotherms reveal some decrease in microporosity and generation of mesoporosity during steaming of the high silica LC-SAPO-34-B at 923 K and during steaming of the LC-SAPO-34-A at ≥ 973 K. At the highest steaming temperature (1023 K_20 h), sample B was no longer porous to N_2 and exhibited a single broad ^{29}Si ssNMR resonance at −116 ppm in panel (D). By contrast, the structural transformation to a dense SAPO phase (structure thought to be related to tridymite) was completed in much shorter duration compared to the SAPO-34 CP7129 (1023 K_113 h) exposed to the same steaming temperature.

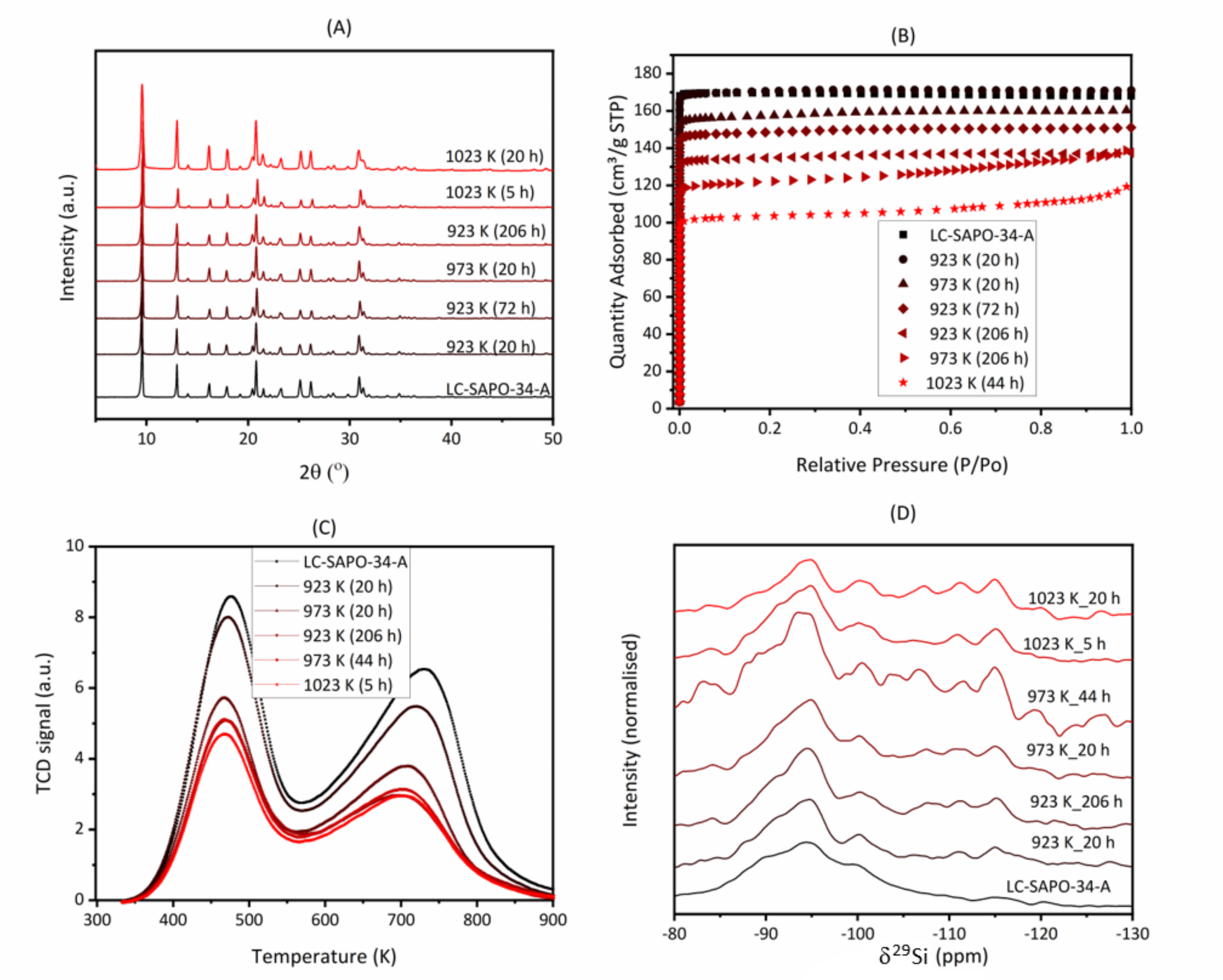

Figure 8. LC-SAPO-34-A steamed at 923–1023 K between 5–206 h. (A) PXRD patterns; (B) N_2 isotherms at 77 K, revealing the development of mesopores at 973 K (206 h); (C) NH_3-TPD profiles normalised against mass and (D) ^{29}Si MAS-ssNMR spectra normalized by mass and number of scans.

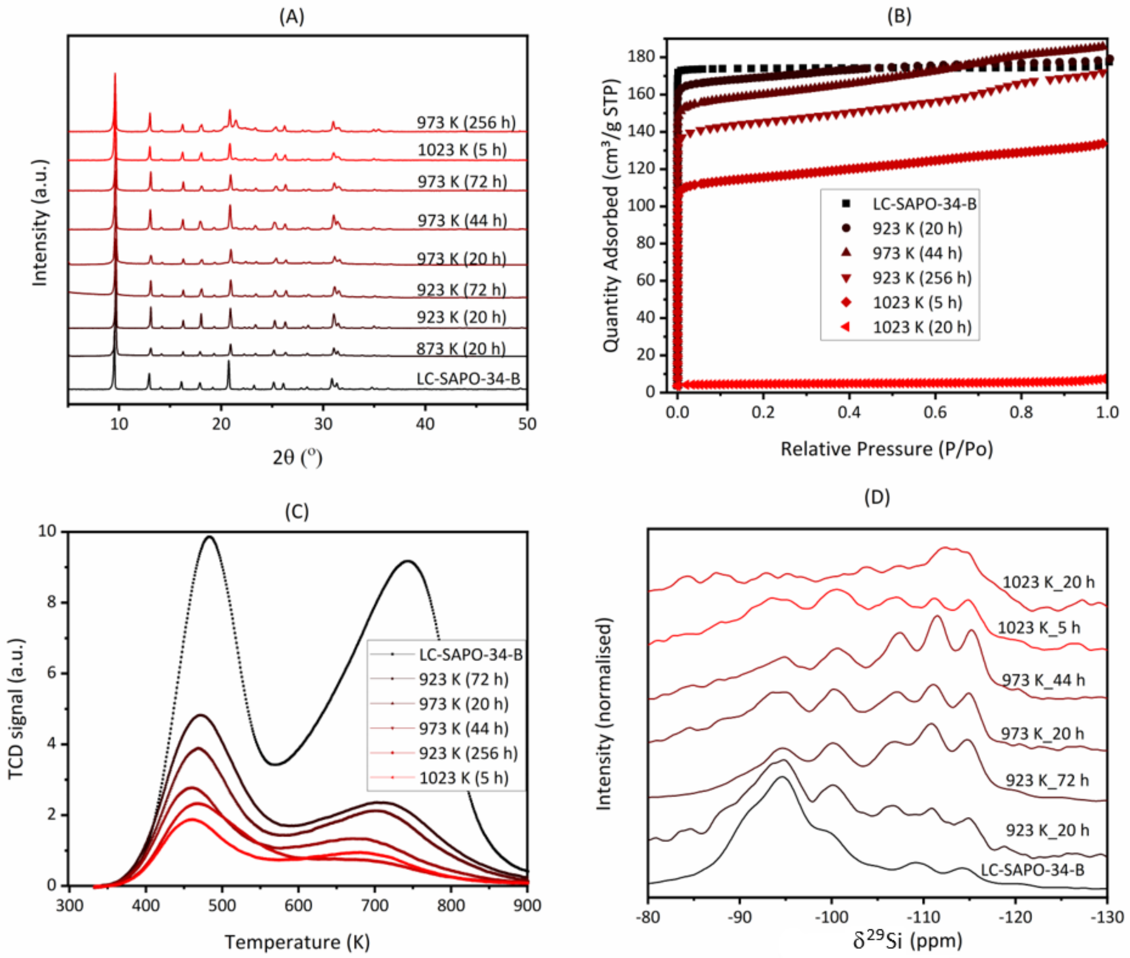

Figure 9. LC-SAPO-34-B steamed at 923–1023 K between 5–256 h. (A) PXRD patterns; (B) N_2 isotherms at 77 K, revealing the development of mesopores at 973 K (20 h); (C) NH_3-TPD profiles normalised against mass and (D) ^{29}Si MAS-ssNMR spectra normalized by mass and number of scans.

Viewed under the optical microscope, both sets of large crystals develop a less transparent core after steaming. The core is evident even under mild steaming conditions and increases in size and opacity with progressive steaming (Figure 10). The optical images capture multiple crystals and show that the size of the dark core varies from crystal to crystal. The core size depends on the overall crystal size, with small crystals containing small cores. Thus, the core size is related to the availability of elements, rather than the distance the steam can penetrate from the outside of the crystal.

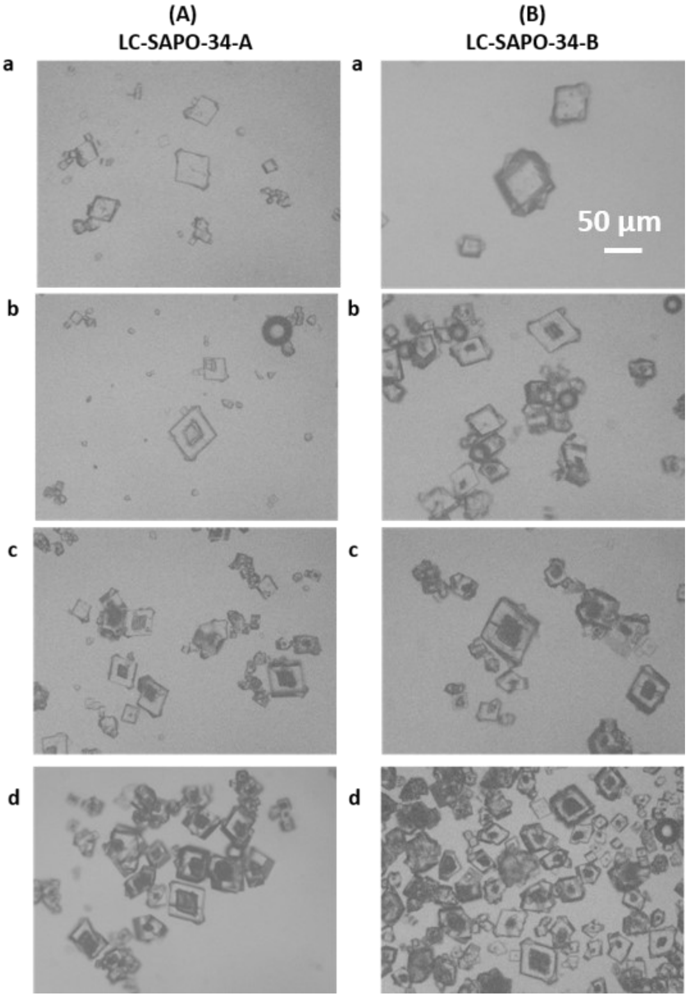

Figure 10. Optical images collected in transmission showing the development of dark patches in the steamed (A) LC-SAPO-34-A and (B) LC-SAPO-34-B. Crystal size varies from 10 to 100 microns. Calcined SAPO-34 (images **a**) and steamed SAPO-34 for 20 h at 923 K (images **b**), steamed at 973 K for 20 h (images **c**) and at 973 K for 44 h (images **d**) for the corresponding large crystal LC-SAPO-A and LC-SAPO-B, respectively.

To investigate this observation further, SEM images were obtained on a lightly crushed crystal of sample LC-SAPO-34-A steamed for 20 h at 973 K that had broken open (Figure 11). A terraced morphology can be seen around the edges of the core, typical of a fracture surface of a crystalline material, whereas the core appears to have a much more irregular structure. In both crystals, there is what appears to be a crystalline nucleus at the centre of the core. At the interface between core and rim regions, and also within the rim, there are features suggestive of material transport. These results therefore suggest some degree of degradation of the crystal structure of the original materials with a densification of material in the cores. We speculate that the transformation occurring in the core is triggered by defects acting as nucleation points.

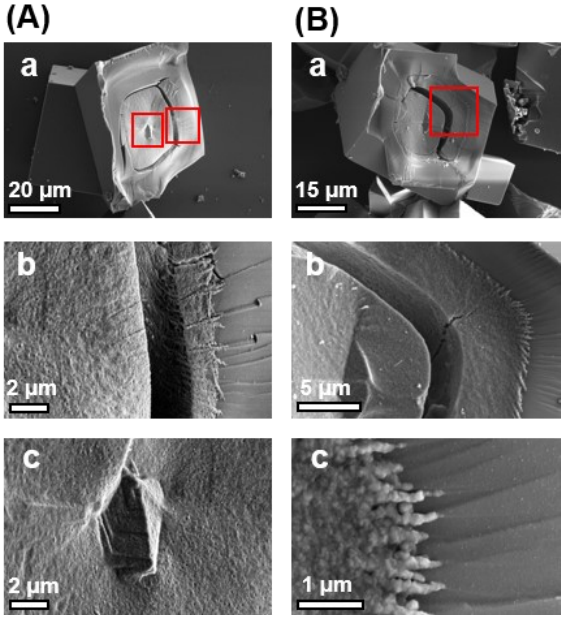

Figure 11. SEM images obtained at three different magnifications on two lightly crushed crystals: crystal (A) and crystal (B) both from the same batch of sample LC-SAPO-34-A steamed for 20 h at 973 K.

Selected single crystals were studied by FIB-SEM where it was possible to cross-section crystals to reveal the cores (Figure 12). The SEM images suggest that the optically dark patches are related to the presence of meso- and macropores, which appear as the dark areas in the images and extend over similar proportions of the exposed face to the dark optical zones. In images (B) and (C), the porous regions cover ~20 % of the crystal cross-section, whereas a slightly smaller proportion of 15 % is found from Figure 12. SEM images were obtained on another crystal of sample LC-SAPO-34-B-973-44 (Figure 12D) which also contained large meso- and macropores, but in that case they were more dispersed throughout the crystal.

A histogram of pore area, measured from selected SEM images, in Figure S11 shows that all 3 samples of large crystals have cross sectional pore areas concentrated in the 10^{-3} to 10^{-1} μm^2 range (i.e. dimensions of the order of 10s to 100s of nanometers) and the total pore areas occupy ~ 2–5 % of the exposed cross-sectional area. The exposed cross sections were analysed by EDX (at 5 kV), showing homogeneous distributions of Si, Al and P (Figure S12), indicating that on the micron scale there was no net Si migration within the structure and any segregation or agglomeration of Si is not resolvable at this length scale. Therefore, coupled with the ^{29}Si ssNMR showing changes in the Si environments, this suggests much more localised alterations of the Si environment, at nanometer length scales.

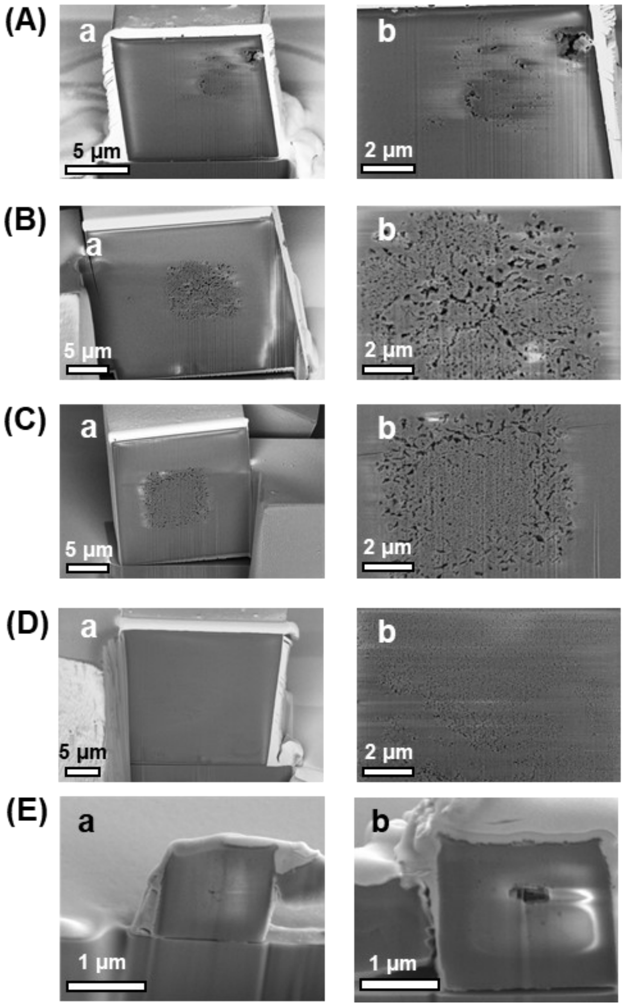

Figure 12. (A) – (D) FIB-SEM images of steamed large crystals at two different magnifications (a and b) showing the cross section through the middle of each crystal: (A) LC-SAPO-34-A-973-20; (B) LC-SAPO-34-B-973-20 and (C-D) two different crystals of sample LC-SAPO-34-B-973-44. The bottom panel (E) shows two different crystals (a) and (b) of sample CP7129-973-20 at the same magnification.

The microcrystalline powder sample CP7129 was also analysed by the same FIB-SEM technique: two crystals of the steamed CP7129 (973 K for 20 h) are presented in panel E, Figure 12. The crystal in image **a** has a few pores of ~20-25 nm and those in image **b** on a different crystal from the same batch show some pores that are connected into larger networks in the middle of the crystal. These features for the CP7129 are similar to the changes in the low silica large crystal LC-SAPO-34-A (images in panel A) which was steamed under the same conditions (973 K for 20 h).

As planned, the larger crystals were amenable to SR-IR microspectroscopic investigation, both to examine heterogeneity in the distribution of hydroxyl groups throughout the crystals and also to follow reactivity of methanol, as described later. IR spectra of calcined samples of both LC-SAPO-34-A and LC-SAPO-34-B display a well-defined double resonance at ca. 3600 cm^{-1} (Figure S2) due to OH bands at 3615 and 3594 cm^{-1}. These are assigned to Brønsted acid sites in slightly different local environments [48], and are evenly distributed over the crystals, as shown in Figure 13 for LC-SAPO-34-A.

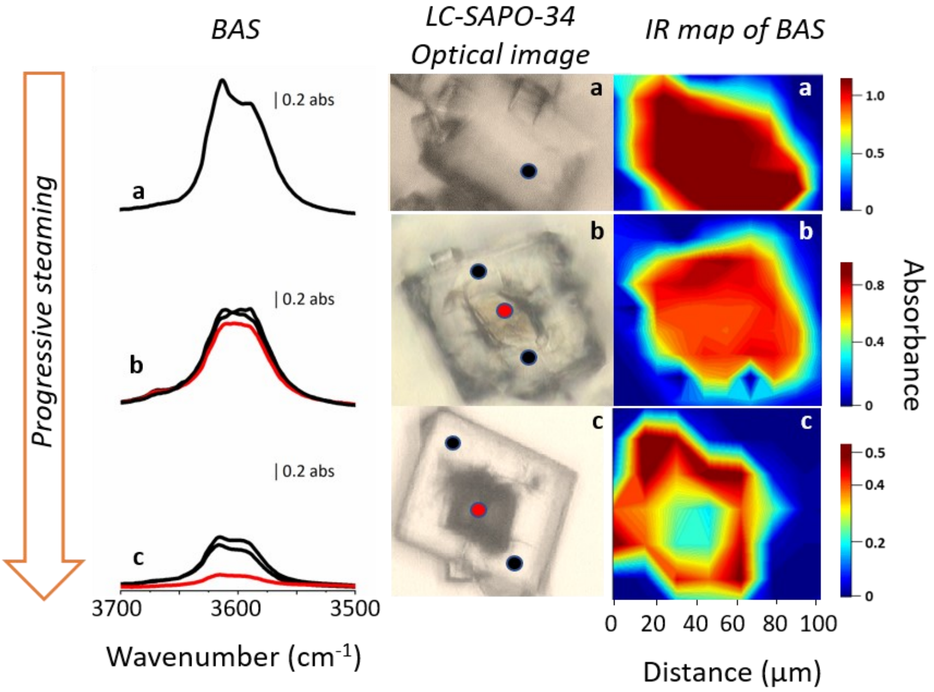

Figure 13. FTIR spectra collected in transmission over the crystal edge (in black) and middle (in red) revealing the dark patches have lost Brønsted acid sites (BAS). Map of the 3600 cm^{-1} hydroxyl band intensity across crystal (a) LC-SAPO-34-A calcined; (b) steamed LC-SAPO-34-A-923-20 and (c) steamed LC-SAPO-34-A-973-20.

Steamed samples display a core in the optical images, which gets more noticeable as the intensity of streaming increases, as shown in Figure 13 for LC-SAPO-34-A. The distribution of OH groups across core and shell can therefore be examined by mapping using an aperture smaller than the core, bearing in mind that the IR measures a projection through the crystal which even over the core will include signal from the rim. After steaming at 923 K (20 h) the core was faintly visible, with the crystal showing slightly less BAS hydroxyls in the IR map in that region. In a crystal of similar size steamed at 973 K for the same duration the effect was much more marked: the absorbance of the hydroxyl peak over the core of the crystal (red spectrum in image **c** of Figure 13), was much lower than over its rim (black spectra in in image **c** of Figure 13). These results show that while the crystal loses some acid sites throughout its rim, most of the acid sites in the crystal core are lost. A different process must therefore occur in the core, which we know from SEM to result in the development of mesopores. If the size of the core in this crystal is representative, this suggests the core makes up a little over 10% of the total volume, and so might account for the loss of microporosity but not for the 30% reduction in BAS in the bulk.

The higher Si sample, LC-SAPO-34-B (16.4 mol% of Si), steamed at 973 K for 44 h, had lost most of its acidity (81% of BAS lost) and displayed a much weaker resonance at ca. 3600 cm^{-1}. In addition, a weak peak at 3672 cm^{-1} was more clearly visible (Figure 14). In studies of SAPO-34 microcrystals Bordiga et al. have assigned minor hydroxyl band components they observed at 3676 cm^{-1} to terminal P-OH species [49].

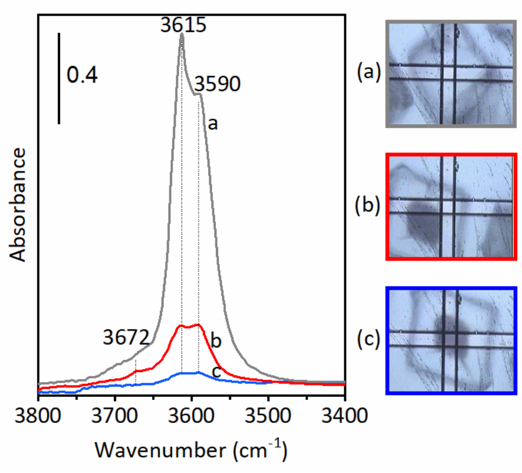

Figure 14. FTIR spectra collected in transmission over (a) LC-SAPO-34-B calcined, (b) steamed LC-SAPO-34-B-973-44 crystal core and (c) steamed LC-SAPO-34-B-973-44 crystal rim, revealing that the core has lost Brønsted acid sites and steaming generates additional defects.

Single crystal diffraction (SCXRD) analyses on crystals from sample LC-SAPO-34B after calcination and after steaming at 973 K for 44 h were performed, and details are given in the SI (Tables S1 and S2). For a representative steamed crystal (which shows an optically dark core) the crystal is still single (i.e. there are no diffraction rings, which would be obtained if it had recrystallized to microcrystalline domains) and no unindexed reflections were observed, although background scattering was higher, suggesting the possibility of a higher proportion of amorphous material. After calcination, the mean 'Al'-O bond distance is 1.691 Å and the mean 'P'-O distance is 1.535 Å. After steaming, the mean 'Al'O- distance became a little shorter, 1.659 Å, and the mean 'P'-O distance lengthened slightly to 1.547 Å (Table S2). These changes in bond lengths are small but significant. The increase in the 'P'-O bond distance is not consistent with a straightforward replacement of Si^{4+} by P^{5+}, (e.g., the reverse of SM2 substitution mechanism) but could suggest the development of some aluminosilicate islands in a random way throughout the structure. A long-range average would in that case see more Si on the Al site (making it smaller) and some Al and Si on the 'P'(P/Si) site, making it larger. However, the results suggest that widespread disordering of tetrahedral cations does not take place.

Additionally, selected samples were examined by Rietveld refinement analysis via powder diffraction of their dehydrated forms (Figures S14, S15, S16 and S17), which gives accurate cell dimensions; details are given in the SI (Table S3). The unit cell volumes of the two calcined materials are very similar: CP7129, 2449.6(5) $Å^3$; LC-SAPO-34-B, 2447.6(5) $Å^3$. These values are slightly higher than the values reported by Arstad et al. [22] for their calcined sample (7% Si = 2430.7(3) $Å^3$). Table S2 reveals a contraction of the unit cells after steaming by 12 $Å^3$ and 40 $Å^3$ for CP7129 and LC-SAPO-34-B, respectively, under mild and moderate conditions. Arstad et al. [22] also reported a contraction by 8 $Å^3$ after steaming their 7% Si sample. The larger unit cell contraction for the LC-SAPO-34-B steamed at 973 K for 44 h is due to the higher Si content in this large crystal sample, making it more susceptible to steaming under these conditions. Although the detailed local structure of the steamed samples remains an open question, we speculate that the unit cell contraction is a consequence of the overall shortening of T-O bond lengths which results from the observed loss of Brønsted acid sites. In zeolites, for example, the presence of protons in bridging hydroxyls has been observed and modelled to result in the lengthening of Si-O and Al-O bond lengths [50-52].

Additionally, some minor reflections (at 2θ values of 21.4, 24.8, 36.0 and 48.8°) were observed, indicating a small amount of recrystallization to a dense phase had occurred.

3.3 Catalytic Performance in the MTO Reaction

The catalytic performance in the MTO reaction was measured at 723 K for the calcined and steamed CP7129 sample (panels A to D) and the two large crystal samples (panels E and F) in Figure 15. A more dilute methanol feed (40%) was used for the large crystals, to prolong their reaction lifetime, and so their total hydrocarbon conversion before deactivation was much lower (Figure S18).

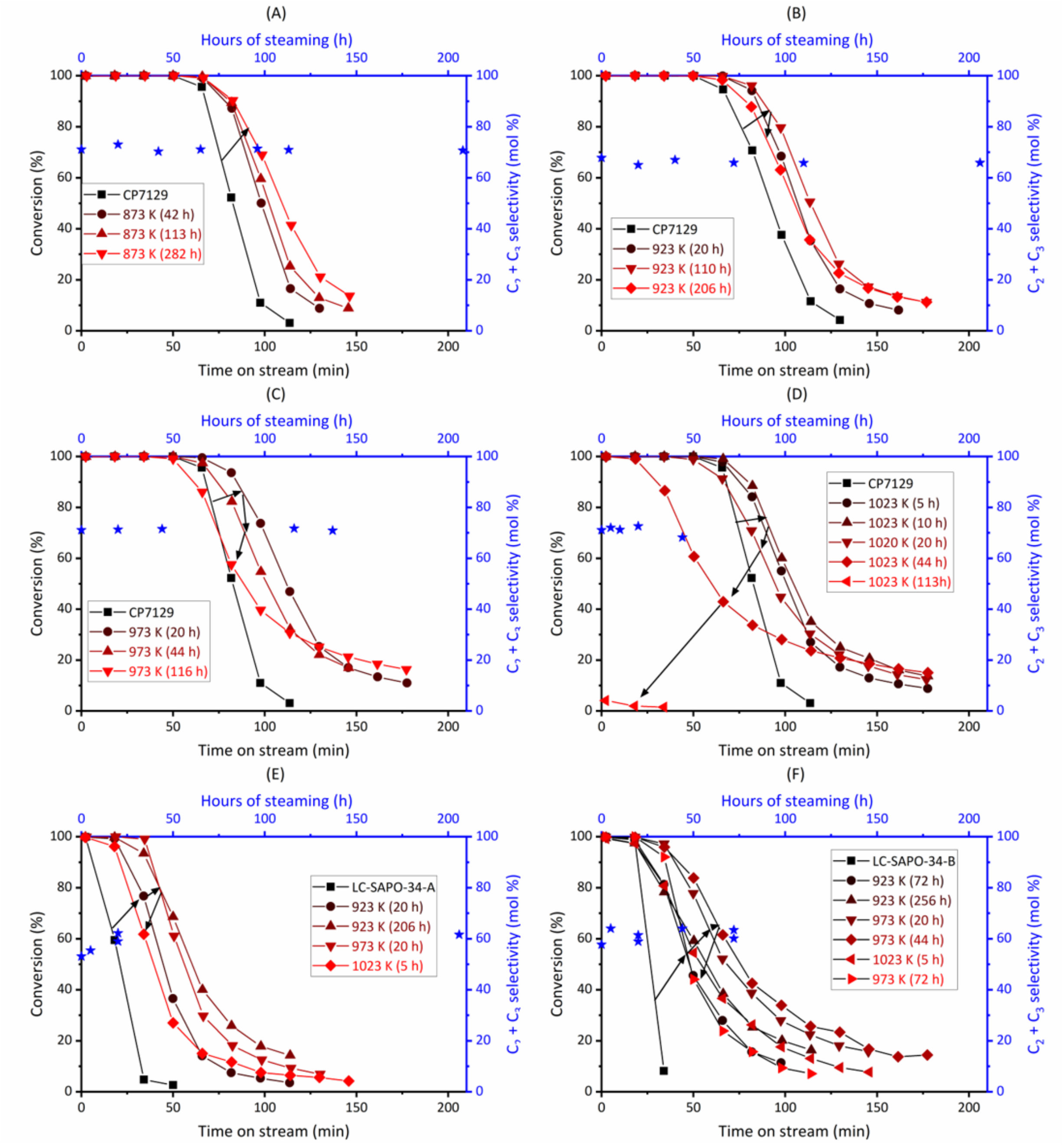

Figure 15. MTO catalytic conversion at 723 K for (A-D) CP7129 at WHSV = 7 h^{-1} and (E-F) large crystals LC-SAPO-34-A and –B tested at WHSV = 3 h^{-1} using a more dilute methanol and water feed. The arrows follow the changes in the conversion curves. Blue stars mark the summed C_2 and C_3 selectivity (via the right-hand *y*-axis label and the *x*-axis label above).

At every temperature, some degree of steaming improves the performance of the catalysts in terms of their 'lifetime' (total methanol conversion per gram of catalyst). For the more vigorous conditions (923 K and above) the lifetime increases to a maximum, after which further steaming results in a decline in performance. This is most marked for the highest temperature, 1023 K.

The microcrystalline CP7129 catalysts convert methanol to light olefins (ethylene + propylene) with a summed selectivity of around 70 mol%, close to that reported (75-80%) for the optimised fixed bed MTO process [4], and this varies little with steaming conditions or temperature. The large crystal batches, which were examined with a reduced WHSV and with a mixture of methanol with water, show summed selectivity closer to 60%. The selectivity to light olefins is thought to depend mainly on the cage structure (rather than the acidity) of the microporous catalyst [8,9,53]. In particular, Kang et al. suggest that the light olefin selectivity depends on the size of the ring in the cage that limits the size of the polymethyl aromatic intermediate to olefin generation [53].

The overall ethylene/propylene ($C_2^=/C_3^=$) product ratio for CP7129 is 1.1, regardless of steaming conditions, and for large crystal batch LC-SAPO-34-A it is 1.0. These values are within the range 0.7-1.2 reported previously for SAPO-34 catalysts under fixed bed conditions [3,4,8,9]. There is for all CP7129 samples (before and after steaming) an increase in the $C_2^=/C_3^=$ ratio from ca. 0.7 to 1.2 during the active phase of the MTO reaction (where the conversion is 100%) followed by a decrease during the deactivation (Figure S19). The increase in the ethylene selectivity with time on stream has been observed previously [9,54,55] and attributed to increased steric constraints resulting from coke formation in the *cha* cages resulting in diffusion resistance to product molecules.

3.4 Coke formation during the MTO reaction

After deactivation during MTO catalysis, the carbonaceous coke retained was investigated by TGA. The amount of coke retained in each sample and the first derivatives of the TGA curves are given in Figure S20 for samples pre-steamed under different conditions. For the CP7129 sample the amount of deposited coke is higher and the coke less refractory in those catalysts that have been subject to steam treatment, up to extended treatment at 1023 K, when the catalysts lose their acidity and microporosity. In the best performing catalysts, the coke levels reach ca. 20%, compared to 16.2% on the calcined material. We speculate that in the samples with higher concentrations of acid sites, there are more reactions (methylation, ring closure etc.) occurring on the same coke molecules leading to a more graphitic/refractory coke and subsequent pore blocking. When the active sites are further apart in the steamed materials, more of the crystals volume can be utilised before the pores become blocked. At the highest steaming temperature (1023 K, 44 h) for the CP7129, the amount of coke retained is reduced due to the significant loss of acidity and additional loss of micropore volume. The amount of coke formed on the calcined large crystals is much lower than on the powder (5-6 wt% in calcined samples). This is because the diffusion distances from surface to active sites become much larger, and the material is more prone to pore blocking in the region close to the crystal surface, leading to deactivation, as reported previously [56]. As a corollary, the increase in the amount of coke retained in the steamed large crystals is more notable. Even though the large crystals deactivate 17× faster than the microcrystalline sample, the improvement in accessibility of the large crystals (where the coke increases by a factor of 2) is greater than the improvement due to steaming in the small crystals (1.25×), which is consistent with the increased lifetime as more of the crystal is being utilized.

3.5 Structural and physicochemical changes during steaming and their effect on MTO catalysis performance

The effect of steaming on the CP7129 at different temperatures is summarised in Figure 16. 16. Trendlines for the micropore volume, lifetime (methanol conversion to hydrocarbons per gram of zeolite), Brønsted acid sites (derived from the NH_3-TPD measurements) and isolated Si relative to the calcined material are shown as a function of steaming time at each temperature. Heating in steam from 873 K up to 973 K results in progressive changes in acid site concentration, ^{29}Si and ^{31}P MAS-ssNMR spectra and microporosity, even while PXRD indicates that SAPO-34 remains highly crystalline and there is only very minor formation of other crystalline phases.

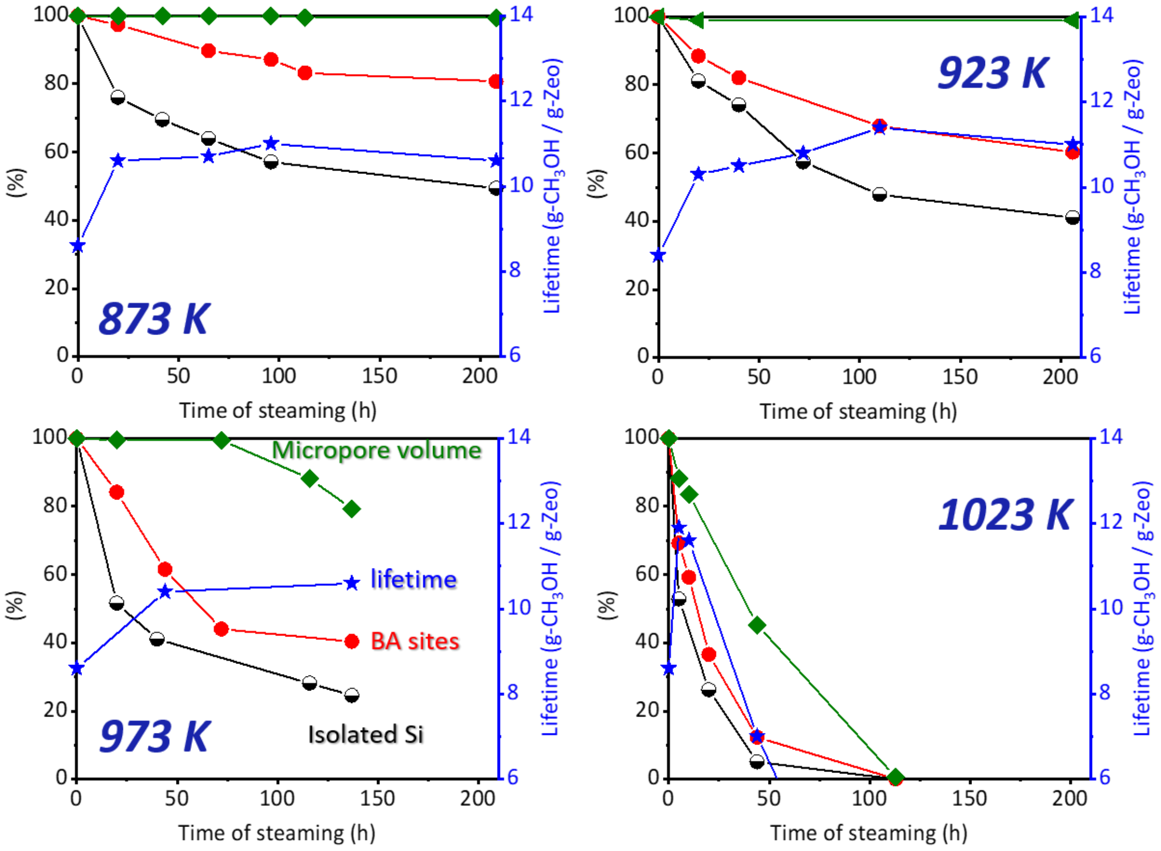

Figure 16. Effect of the steaming temperature of SAPO-34 CP7129 on its acidity (BAS as measured by NH_3-TPD and isolated Si as measured by the Si(OAl)$_4$ peak in the ^{29}Si MAS-ssNMR spectrum) and micropore volume (BET surface area expressed as % relative to the non-steamed CP7129, green trace). To the ordinate axis on the right (blue axis) is the MTO lifetime for each sample (amount of methanol converted to hydrocarbons per gram of zeolite sample).

Only under the most severe conditions studied does recrystallization occur to a significant degree. Loss of BAS and the related reduction in the isolated Si species, as measured by the $Si(OAl)_4$ peak in the ^{29}Si MAS-ssNMR spectrum, occur over similar timescales, although the former (which is measured more quantitatively) reduces more dramatically in relative terms (Figure 16). The loss of Si from this $Si(OAl)_4$ environment in the CHA structure (ca. 1 Si per cage) is achieved without reduction in microporosity or crystallinity. Under the harshest steaming conditions, a rapid loss of BET surface area occurs due to the phase transformation of SAPO-34 to a dense phase.

The pattern of structural change in the larger crystals is similar to that observed for the microcrystalline powder, but occurs more rapidly for these samples, and fastest for the material with higher Si content. Furthermore, the different physical changes in each material do not all take place at the same rate. For example, for the CP7129, over 50% of the Brønsted acid sites are lost after steaming at 973 K for 72 h, for example, by which time there has been no significant loss in microporosity or crystallinity. For the larger crystals, the changes in ^{29}Si MAS-ssNMR and microporosity occur more readily, and it is not easy to observe samples where the former changes while the latter does not. Nevertheless, for sample B, similar upfield (more negative ppm) ^{29}Si peaks are observed clearly after 923 K for 20 h, when only *ca* 10% of the microporosity has been lost.

Increases in intensity of resonances in the upfield region at lower ppm of the ^{29}Si MAS-ssNMR spectra are observed with increasing duration of steaming. The ^{29}Si MAS-ssNMR of the microcrystalline sample steamed at 923 K for up to 206 h shows significant Si redistribution has occurred, giving six resonances at −94.5, −101, −107, −111, −115 and −121 ppm. Notably, no reduction in microporosity was measured for this material, and similar behavior was seen for shorter steaming times at 973 K. The development of such peaks is often interpreted in terms of the growth of Si islands but, as reported by Arstad et al. [22] the chemical shifts measured consistently in our spectra cannot straightforwardly be interpreted as the silicon islands found in SAPOs made by direct synthesis. We consider two possible models for the Si atoms in these new environments (*ca*. 5-10% of the total tetrahedral cation content). In the first, Si and (some P) atoms leave the framework and react to form a non-crystalline phosphosilicate; in the second, the environments result from silicon islands within the SAPO-34 framework. For the second model, the difference in chemical shift of the observed resonances from those expected for Si islands in SAPO-34 on the basis of observations of calcined materials with high Si contents (as discussed by Arstad et al. [22]) could be due to their origin in the presence of steam at very high temperature. This could lead to a high energy distribution of P atoms within or around the

Si islands which causes the ^{29}Si MAS-ssNMR resonances to be shifted to more negative values (−115 and −120 ppm) compared to the $Si(OSi)_4$ species in calcined SAPO-34 (−110 ppm). These new upfield resonances are not from Si close to OH (^{1}H-^{29}Si CP MAS-ssNMR of Arstad et al. [22]). While generally thought to be unfavourable in as-prepared SAPOs, Si-O-P bonds exist in phosphosilicate glasses, as reported by Coelho et al. [57] where the ^{29}Si MAS-ssNMR peak is at −121 ppm, consistent with the most negative peak seen in both their and our steamed SAPO-34 samples.

For the large crystals, additional insight is available from different forms of microscopy, which show that a rim and core texture develops, beginning at 923 K and becoming more noticeable at higher temperatures (973 K). In LC-SAPO-A, after steaming at 923 K for 20 h there is some evidence for darkened cores and some development of additional ^{29}Si MAS-ssNMR resonances, a minor loss of BAS and no loss of microporosity, whereas at 973 K for 20 h the core is well developed, showing meso/macroporosity and evidence of material transport at the core/rim interface. Furthermore, IR indicates loss of OH throughout the crystals of this sample, but almost complete loss in the core, while there is some loss of microporosity at this stage (ca 6%). Furthermore, close investigation of the microcrystals of CP7129 indicates macropore development, and by extrapolation that similar 'core-shell' structures can develop in that material.

The features of steamed SAPO-34 crystals most relevant to their catalytic performance are the reduction in Brønsted acid concentration without loss of microporosity, followed by the development of cores that lose most or all acidity and, we speculate, microporosity. The effect of steaming temperature on catalytic performance was studied in detail for CP7129 (Figures 15 and 16). Steaming at or below 923 K causes local structural rearrangements in the Si distribution, but the micropore volume is retained despite a 40% reduction in the number of active sites via an activated process with E_{act} of 146(18) kJ mol^{-1}. At 973 K there is a loss of 60% of the acid sites up to 100 h, with only a small decrease in porosity (10%) and little reduction in the reaction lifetime. These data indicate that the steaming temperature should be kept below 973 K (<100 h) to retain full crystallinity and micropore volume when performing accelerated aging studies to simulate the active catalyst. This is significant for optimal study of the degradation process in these materials. The loss of acid sites and then microporosity is faster in the large crystal samples, at least in part because of their higher Si content, as shown in the graphical summary of Figure 17.

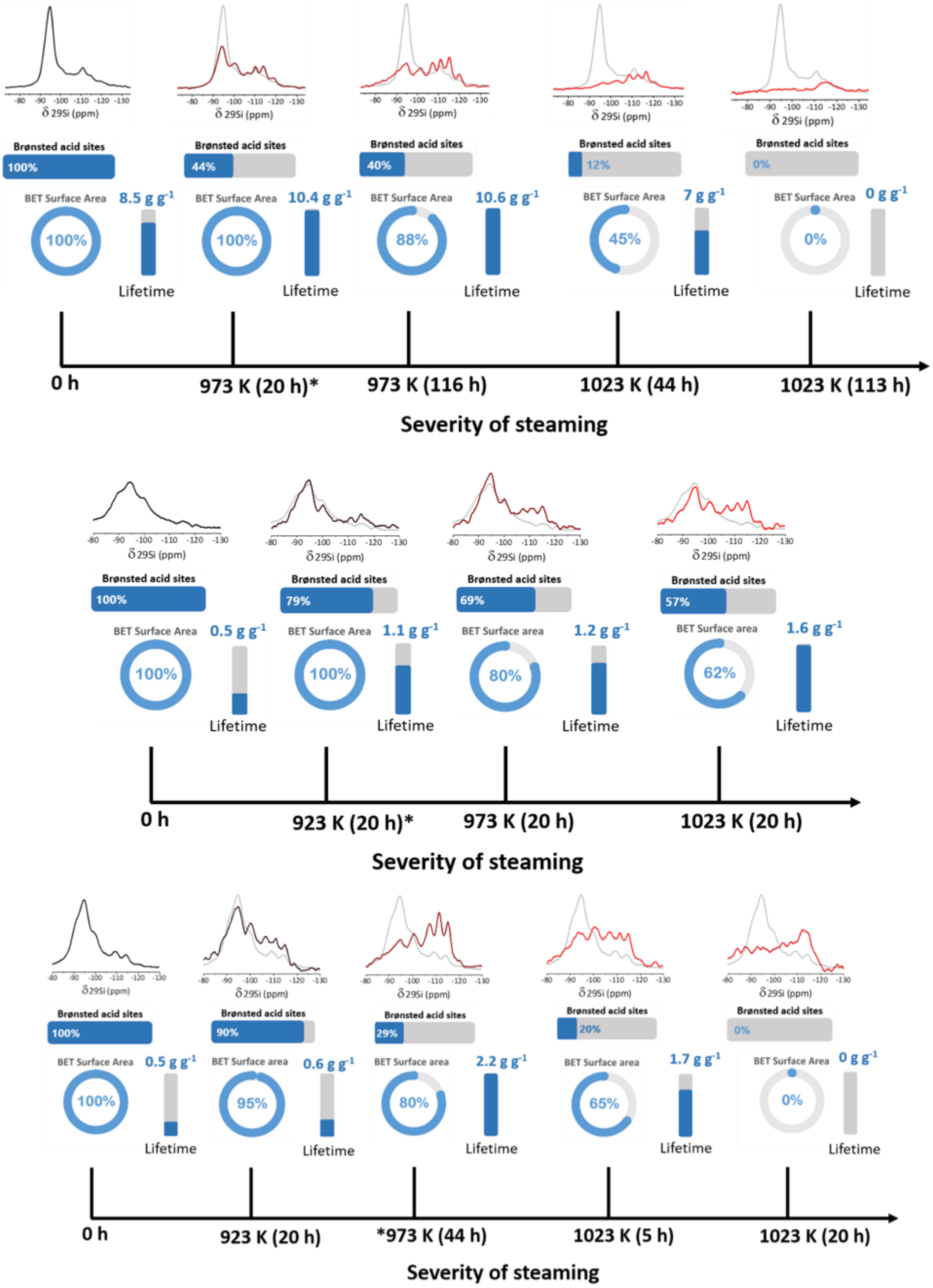

Figure 17. Schematic representation of effects of steaming on Top, CP7129; Middle, LC-SAPO34-A; Bottom, LC-SAPO34-B. * Indicates sample analysed by FIB-SEM.

This emphasizes that the lifetime in MTO catalysis is improved in all cases by steaming, even though a significant amount of BAS (and even some microporosity) is lost. For example, in LC-SAPO-34-A the lifetime is still increasing under the most severe conditions used (1023 K_20 h) while in LC-SAPO-34-B, the maximum lifetime is reached at less severe steaming conditions than for LC-SAPO-34-A, because the disruption of the structure is faster. Even at its optimal lifetime (973 K_44 h), N_2 adsorption isotherms for sample B (Figure 9) show loss of microporosity and formation of mesoporosity, which is also evident in the FIB-SEM cross section images (Figure 12) and histograms (Figure S11). The improvement in lifetime in sample B over the calcined form is preserved even when the core is degraded at 1023 K for 5 h, which shows a large (35%) loss in micropore volume and acid site (80% loss).

These measurements show that the reduction in acid site concentration, which results from the change in the Si environment, is the most important factor in improving the lifetime. For the CP7129 the total hydrocarbon yield is improved by a factor of 1.25× by short duration steaming. A larger relative improvement is observed upon steaming the large crystals LC-SAPO-A and LC-SAPO-B samples deactivate much faster in microcatalytic tests than the microcrystalline sample, but the improvement of steaming the large crystals (4.4×) is greater than that due to steaming the small crystals. The improvement of performance correlates with the reduction in the rate of formation of inactive coke that blocks the pores. The larger crystals are much more susceptible than the powder to blocking because of the large diffusional distances involved, so the improvement is greater.

3.6 *Operando* SR-IR microspectroscopy studies on LC-SAPO-34

The LC-SAPO-34 crystals are of sufficient size and quality to be amenable to SR-IR. The advantages of this synchrotron method over conventional FTIR are discussed elsewhere [58,59], and a detailed SR-IR study of the mechanism of the early stages of the MTO and DMTO reactions over calcined LC-SAPO-34-A, which occurs via the reaction sequence (DME)-methoxy groups-alkenes-hydrocarbon pool, will be reported in detail separately [60]. Here we compare the activity of steamed and calcined LC-SAPO-34-A and LC-SAPO-34-B for methanol and DME conversion over the large crystals by *operando* SR-IR (with on-line mass spectrometry) via a range of different experiment types (pulses vs continuous flow, isothermal vs temperature jump experiments). The aim was to study the effect of steaming on the formation and reactivity of methoxy groups and crystal accessibility and deactivation during the MTO/DMTO reaction.

Four stages can be distinguished for all LC-SAPO-34 crystals when a pulse of methanol is added: DME formation (and desorption), induction period before formation of hydrocarbon products, active catalysis for olefins, and deactivation [60]. Initial addition of methanol results in loss of Brønsted acid sites (Figure 18) and DME formation, which is then desorbed as seen in Figure S21. During the induction period, the concentration of Brønsted acid sites gradually decreases until it reaches a constant level, and surface methoxy groups (SMS) become apparent (Figures S21 and 18).

After a certain induction time, the free BAS concentration begins to increase and there is a change in the CH region as the methoxy groups are replaced by oligomeric species (Figure 19), as the first C-C bonds are formed in the active period, and small olefins are evolved. Additional pulses result in an increase of the concentration of oligomeric species seen by IR, and further evolved olefins, and this continues until the crystals become deactivated.

Figure 18 shows that steaming at 973 K increases the length of the induction period in the crystals, as seen from the time dependence of the OH intensity, and this effect is more noticeable for the LC-SAPO-34-B sample which is more susceptible to steaming, and from which almost all acid sites have been removed. Figure S21 shows the evolution of the ν(CH) region for calcined, mildly steamed and harshly steamed crystals during the trailing edge of the methanol pulse at 573 K as product DME is desorbed, while Figure 19 shows the subsequent spectral evolution after the induction period.

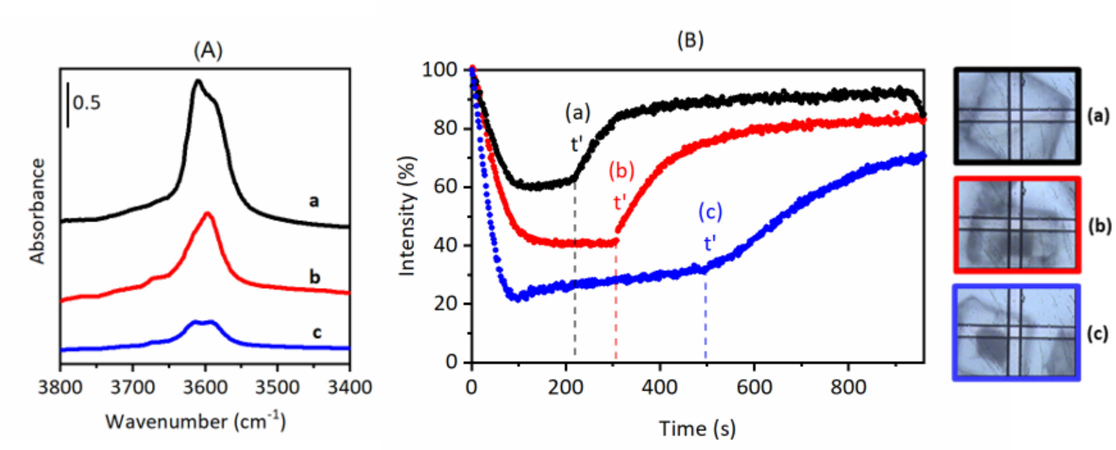

Figure 18. (A) FTIR spectra of dehydrated (a) LC-SAPO-34-A (black), (b) LC-SAPO-34-A-973-20 (red) and (c) LC-SAPO-34-B-973-44 (blue). (B) Time course of the ν(OH) intensity at 3600 cm^{-1} expressed as % relative to the dehydrated crystals during this experiment where an 8 µL pulse of CH_3OH was injected at 573 K. Note, IR spectra in the calcined crystal were measured at the crystal core, while in the steamed crystals, IR spectra were measured at the rim.

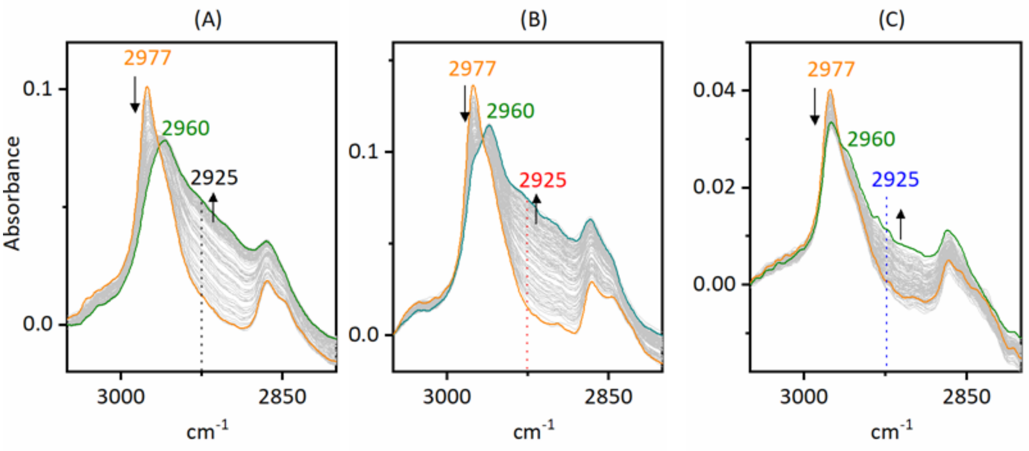

Figure 19. Conversion of SMS during the isothermal methanol experiments at 573 K for sample (A) LC-SAPO-34-A, (B) LC-SAPO-34-A-973-20 and (C) LC-SAPO-34-B-973-44. Synchrotron difference FTIR spectra in the ν(CH) region at 2 s intervals showing the first 200 s during the recovery of OH groups, after the induction period. Spectra are normalised by an offset correction at 3050 cm^{-1}.

After any physisorbed product DME has been removed by purging in N_2 (evident by the loss of bands at 3011, 2945, 2893 and 2836 cm^{-1} in Figure S21) the spectra show bands at 2977 cm^{-1} and 2867 cm^{-1} due to the symmetric and asymmetric vibrations of surface-bound methoxy species

(SMS), as well as residual bands or shoulders at 3030, 2963 and 2845 cm^{-1} assigned to strongly adsorbed DME [51]. The heavily steamed crystals have fewer acid sites and therefore fewer reactive SMS are formed after the DME is removed, compared to the mildly steamed and calcined materials.

After an induction time ($\Delta t'$ in Figure 18) the hydroxyl intensity at 3600 cm^{-1} begins to recover rapidly. As the intensity of the band at 3600 cm^{-1} increases, spectra in the ν (CH) region (Figure 19) indicate the bands from SMS are replaced by a broad envelope of new bands between 2960 cm^{-1} (sharp) and 2870 cm^{-1}. These are attributed to oligomeric hydrocarbons by comparison with spectra observed after separate reaction of propene on the SAPO-34 [60]. To show the time dependence of the growth of oligomeric species during the above methanol experiment, the absorbance at 2925 cm^{-1} (where there is least overlap with the original SMS) was plotted (Figure S22). The time-course of the 2925 cm^{-1} band reveals that the oligomer is growing more gradually in the steamed sample B compared to the calcined non-steamed SAPO-34 crystal A. Therefore, the rate of C–C bond formation is determined by the concentration of methoxy groups, and it is thought that *direct* coupling of SMS is the main C–C coupling route in SAPO-34 in these experiments.

The wide range FTIR difference spectra during an isothermal multi-methanol pulse experiment (573 K) are shown in Figure S23; spectra at the end of each methanol pulse are plotted for each crystal. Despite the reduced acid site density, as evident by a weaker 3600 cm^{-1} band, the two steamed samples are observed to remain active and generate hydrocarbons (the intensity in the CH region remains high).

Comparison of FTIR spectra of a calcined and a steamed SAPO-34 crystal was made after three methanol pulses at higher temperature (623 K), given in Figure S24. At 623 K, the calcined crystal was reactive in the first methanol pulse but no changes in the ν(CH) region were seen thereafter – indicating deactivation had occurred. By contrast, the growing intensity on the ν(CH) region in the steamed crystal indicates improved lifetime and decreased tendency to become blocked, consistent with the improved lifetime of steamed samples in the MTO reaction. The gas phase products evolved during the three methanol pulses in this 623 K experiment were also compared. The calcined samples showed signs of deactivation, while the steamed samples continued to generate propene (Figure S25). This is consistent with the microcatalytic MTO tests where the steamed catalyst showed an enhanced lifetime.

In separate experiments, the distribution of residual hydrocarbon species following the flow of DME-containing N$_2$ at 623 K was mapped for both calcined and steamed SAPO-34 crystals (Figure 20). In both calcined and steamed crystal there is some enrichment of hydrocarbons in the outer part of the calcined crystal, as reported previously [56,61] and attributed to the build-up of species closer to the external surface due to diffusional constraints. A much more marked effect is seen for the steamed sample, because of the presence of the 'core', where there are few (if any) residual Brønsted acid sites and so less DME-to-hydrocarbon conversion. The CH band profile contains similar bands to those observed in the MTO reactions, which are attributed to oligomeric hydrocarbons.

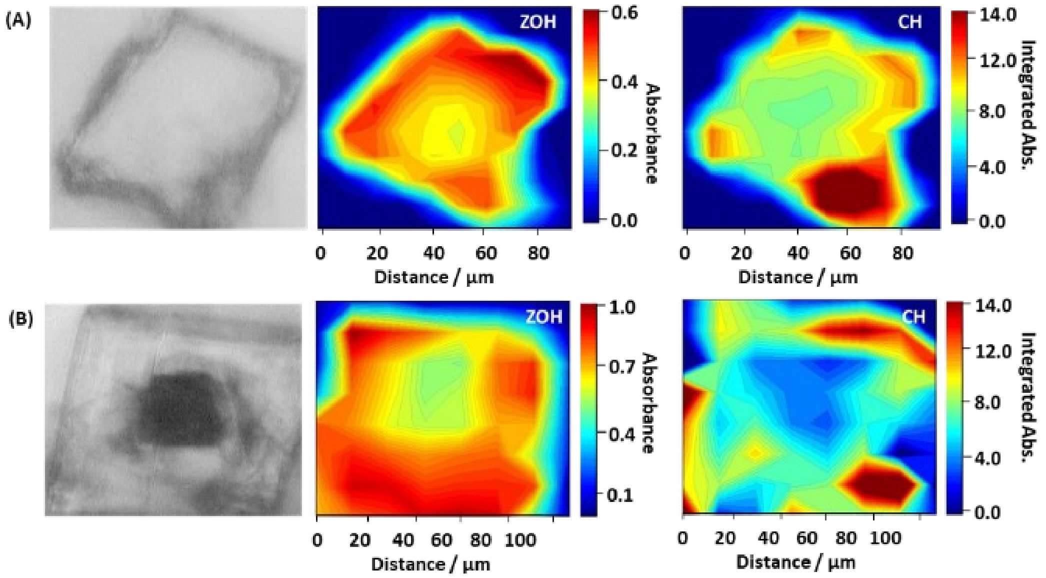

Figure 20. Comparison of calcined LC-SAPO-34-A (A) and steamed LC-SAPO-34-A-973-20 (B), via optical images (left), Synchrotron FTIR concentration maps (right) after exposure to continuous flow of DME in a stream of dry nitrogen at 623 K (30 min) showing the ν(OH) intensity band at 3600 cm^{-1} and the integrated intensity in the ν(CH) region between 2800–3000 cm^{-1}.

In summary, synchrotron FTIR microspectroscopy of LC-SAPO-34 crystals has identified the development of a core with a reduced Brønsted acid site concentration upon steaming. While the entire crystal loses acidity during steaming, the core loses more than the rim and there are no BA sites left in the interior of the crystal after steaming (973 K_20 h). Reaction with methanol (or DME) results in the generation of methoxy groups at the acid sites, and therefore less of these form in the steamed crystals compared to the calcined ones. The induction period ($\Delta t'$) to methanol conversion to propene increases with progressive steaming, and since the mode of reaction of the SMS appears to be the same in each case (a methoxy-methoxy coupling reaction, with simultaneous deprotonation) we speculate that the increased induction time depends in part on the increased diffusion distances required to allow reaction in the steamed samples. Finally, the slower deactivation in steamed samples observed in microcatalytic experiments is mirrored in the SR-IR experiment: the more acid sites, the lower the utilization of the crystal volume in large crystals, as shown by the TGA analyses.

The effect of losing acidity and porosity in the core as observed by microscopy in the large crystals is associated with an irreversible loss of activity in that region. A similar loss of activity is also likely in small crystals which have been steamed at 973 K or above for more than 20 h, since FIB-SEM shows similar structural loss-features in the core. Therefore, the presence of inactive cores indicates the irreversible reduction in the catalytic performance after multiple regeneration cycles, assuming the size of the core formed is sufficiently large relative to the amount of crystal that is utilized during catalytic operation.

4. Conclusions

Steaming the microcrystalline SAPO-34 at 873–1023 K (for 5–256 h) results in the gradual loss of its Brønsted acid sites and a related reduction in the concentration of isolated $Si(OAl)_4$ sites in the framework. The loss of Brønsted acidity can be modelled via a first order process with an activation energy of 146(18) kJ mol^{-1}. Nevertheless, the samples retain crystallinity to PXRD and their microporosity is preserved even when *ca.* half or more of their acid sites are lost. Under these same conditions, solid state MAS-ssNMR indicates redistribution of silicon, which we have speculatively attributed to a high temperature distribution of tetrahedral framework Si, Al and P cations in the SAPO-34 framework. Single crystal X-ray diffraction (SCXRD) shows that the large crystals retain much of their single crystal character upon steaming and that small but significant changes in framework 'Al'–O and 'P'–O framework bond lengths, averaged on the long range, are consistent with the formation of a small amount of 'silicon islands'. Only after steaming at the highest temperature is recrystallization to a dense phase observed.

Examination of the single crystals under the optical microscope indicates the gradual development of optically-darkened parallelepiped ‘cores’ with morphologies related to the crystallographic axes, surrounded by clear rims/shells. These cores are observed even in the early stages of steaming at temperatures above 923 K, when no loss of microporosity is measured, and darken progressively with increasing severity of steaming. The SEM analysis of these steamed crystals, sliced through the cores by ion beam, shows the composition of the solid remains homogeneous on the micron scale over the whole crystal, but reveals the development of meso- and macroporosity, corresponding to local migration of material. This ultimately results in loss of microporosity. FIB-SEM on the microcrystalline CP7129 sample also showed signs of mesopore formation in the crystal cores. Infrared microspectroscopy of steamed crystals shows there is a loss of Brønsted acidity throughout when compared to calcined crystals, but this is most severe in the cores, where all bridging hydroxyls are lost after steaming for 20 h at 973 K.

Microcatalytic testing of SAPO-34 in the MTO reaction indicates the catalytic performance of SAPO-34 in the methanol-to-olefins reactions is improved by moderate steaming, as measured by an increase in catalytic lifetime and yield of hydrocarbon product before deactivation, while the selectivity to ethene and propene is maintained. Also, catalytic testing shows that the large crystal SAPO-34 samples deactivate more rapidly than the microcrystalline material, as expected from literature reports. This is attributed to coke forming close to the external surface and blocking access to a higher fraction of the catalytic sites. Nevertheless, the type of catalysis and the enhancement of catalytic performance by moderate steaming that they display are sufficiently similar to those of the powder sample to indicate they can be suitable model systems to study the steam-induced changes. Furthermore, ^{29}Si MAS-ssNMR, NH_3-TPD and microporosity measurements indicate they evolve structurally in a similar way to powders under the same conditions.

Operando SR-IR microspectroscopic studies on large calcined and steamed crystals of SAPO-34 reveal strong effects of acid site density on the induction time, and the rate of formation of oligomeric hydrocarbon products, even though the reaction mechanism for the first C–C bond formation from surface-bound methoxy species (SMS) appears to be the same. When pulses of methanol vapour are passed over the crystals, hydrocarbon species are found in the rim rather than the core. Careful examination of the adsorption and reaction of methanol at 573 K in the crystalline rims of the mildly steamed crystal shows subtle differences over the time-course of the Brønsted acid sites and the extent of the oligomerization reactions are more gradual down due to lower active site concentrations.

Analysis of the effect of steaming on these large SAPO-34 crystals give important insights into their materials chemistry under conditions relevant to their application in catalysis via techniques that are not readily applicable to powders. In particular, the microscopic imaging techniques reveal for the first time crystal heterogeneity caused by irreversible structural changes. These include the development of meso- and macroporosity and the localized loss of Brønsted acid sites in optically darkened crystalline cores. These irreversible changes also occur in microcrystalline catalyst samples, so that it will not be possible to regenerate those materials fully after use.

Acknowledgments

IBM has received funding from the Engineering and Physical Sciences Research Council (EPSRC, Centre for Doctoral Training in Critical Resource Catalysis, EP/I017008/1) and Scotland's Chemistry departments (ScotCHEM). IBM would like to thank ScotCHEM for the researcher mobility grant towards an industrial placement abroad. IBM also received a scholarship from the SCI and Santander. Johnson Matthey is thanked for in-kind contributions and hosting IBM in their R&D labs. ABN gratefully acknowledges support from the EPSRC (grants EP/L017008/1 and EP/R023751/1). Diamond Light Source is thanked for provision of beam time and support facilities at the MIRIAM beamline B22 (Experiments SM20906-1, SM23471-1 and SM23471-2). We would like to thank the scientists at B22, Dr Mark Frogley and Dr Gianfelice Cinque from the Diamond Light Source as well as Dr Santhosh Matam at the Catalysis Hub and Dr Kathryn Welsby for their assistance with synchrotron IR data acquisition. Finally, we want to extend thanks to Prof Russell F. Howe from the University of Aberdeen for invaluable scientific contributions during our synchrotron sessions and infrared data analysis. Researchers from Johnson Matthey (Maria Villegas, Justin Cribbs, Daniel Gilleland and Ron McHenry) are gratefully acknowledged for their help with the use of physicochemical analytical equipment. The research data supporting this publication can be accessed at: https://doi.org/10.17630/09ddc03e-f121-4e79-9b55-674f64d9c8c4 [62].

References

[1] M.R. Gogate, Methanol-to-olefins Process Technology: Current Status and Future Prospects, Petrol. Sci. Technol. 37 (2019) 559–565. https://doi.org/10.1080/10916466.2018.1555589.

[2] P. Tian, Y. Wei, M. Ye, Z. Liu, Methanol to Olefins (MTO): From Fundamentals to Commercialization, ACS Catal. 5 (2015) 1922–1938. https://doi.org/10.1021/acscatal.5b00007.

[3] W. Song, Y. Wei, Z. Liu, Chemistry of the Methanol-to-Olefins Conversion, in Zeolites in Sustainable Chemistry, Eds. F.-S. Xiao, X. Meng, Springer-Verlag, Berlin, Heidelberg 2016, 299-346. https://doi.org/10.1007/978-3-662-47395-5

[4] J.Q. Chen, A. Bozzano, B. Glover, T. Fuglerud, S. Kvisle, Recent Advancements in Ethylene and Propylene Production using the UOP/Hydro MTO Process, Catal. Today 106 (2005) 103-107. https://doi.org/10.1016/j.cattod.2005.07.178

[5] C. Baerlocher, L.B. McCusker, D.H. Olson, Atlas of Zeolite Framework Types, 6th rev. ed, Elsevier, Amsterdam, 2007.

[6] W. Song, J.F. Haw, J.B. Nicholas, C.S. Heneghan, Methylbenzenes are the Organic Reaction Centers for Methanol-to-Olefin Catalysis on HSAPO-34, J. Am. Chem. Soc. 122 (2000) 10726–10727. https://doi.org/10.1021/ja002195g.

[7] B. Arstad, S. Kolboe, The Reactivity of Molecules Trapped within the SAPO-34 Cavities in the Methanol-to-Hydrocarbons Reaction, J. Am. Chem. Soc. 123 (2001) 8137–8138. https://doi.org/10.1021/ja010668t.

[8] U. Olsbye, S. Svelle, M. Bjørgen, P. Beato, T.V.W. Janssens, F. Joensen, S. Bordiga, K.P. Lillerud, Conversion of Methanol to Hydrocarbons: How Zeolite Cavity and Pore Size Controls Product Selectivity, Angew. Chem., Int. Ed. 51 (2012) 5810–5831. https://doi.org/10.1002/anie.201103657.

[9] B.P.C. Hereijgers, F. Bleken, M.H. Nilsen, S. Svelle, K.-P. Lillerud, M. Bjørgen, B.M. Weckhuysen, U. Olsbye, Product Shape Selectivity dominates the Methanol-to-Olefins (MTO) Reaction over H-SAPO-34 Catalysts, J. Catal. 264 (2009) 77–87. https://doi.org/10.1016/j.jcat.2009.03.009.

[10] J. Tan, Z. Liu, X. Liu, X. Han, C. He, R. Zhai, Crystallization and Si Incorporation Mechanisms of SAPO-34, Micropor. Mesopor. Mat. 53 (2002) 97–108.

[11] R. Vomscheid, M. Briend, M.J. Peltre, P.P. Man, D. Barthomeuf, The Role of the Template in Directing the Si Distribution in SAPO Zeolites, J. Phys. Chem. 98 (1994) 9614–9618. https://doi.org/10.1021/j100089a041.

[12] G. Sastre, D.W. Lewis, C.R.A. Catlow, Modeling of Silicon Substitution in SAPO-5 and SAPO-34 Molecular Sieves, J. Phys. Chem. B. 101 (1997) 5249–5262. https://doi.org/10.1021/jp963736k.

[13] T. Fjermestad, S. Svelle, O. Swang, Mechanism of Si Island Formation in SAPO-34, J. Phys. Chem. C. 119 (2015) 2086–2095. https://doi.org/10.1021/jp510845z.

[14] G. Sastre, D.W. Lewis, C.R.A. Catlow, Structure and Stability of Silica Species in SAPO Molecular Sieves, J. Phys. Chem. 100 (1996) 6722–6730.

[15] D. Barthomeuf, Topological Model for the Compared Acidity of SAPOs and Zeolites, Zeolites, 14 (1994) 394–401. https://doi.org/10.1016/0144-2449(94)90164-3.

[16] R. Martínez-Franco, Z. Li, J. Martínez-Triguero, M. Moliner, A. Corma, Improving the Catalytic Performance of SAPO-18 for the Methanol-to-Olefins (MTO) Reaction by Controlling the Si Distribution and Crystal Size, Catal. Sci. Technol. 6 (2016) 2796–2806. https://doi.org/10.1039/C5CY02298C.

[17] J. Goetze, F. Meirer, I. Yarulina, J. Gascon, F. Kapteijn, J. Ruiz-Martínez, B.M. Weckhuysen, Insights into the Activity and Deactivation of the Methanol-to-Olefins Process over Different Small-Pore Zeolites as Studied with Operando UV–vis Spectroscopy, ACS Catal. 7 (2017) 4033–4046. https://doi.org/10.1021/acscatal.6b03677.

[18] W. Dai, G. Wu, L. Li, N. Guan, M. Hunger, Mechanisms of the Deactivation of SAPO-34 Materials with Different Crystal Sizes Applied as MTO Catalysts, ACS Catal. 3 (2013) 588–596. https://doi.org/10.1021/cs400007v.

[19] I. Lezcano-Gonzalez, E. Campbell, A.E.J. Hoffman, M. Bocus, I.V. Sazanovich, M. Towrie, M. Agote-Aran, E.K. Gibson, A. Greenaway, K. De Wispelaere, V. Van Speybroeck, A.M. Beale,

Insight into the Effects of Confined Hydrocarbon Species on the Lifetime of Methanol Conversion Catalysts, Nat. Mater. 19 (2020) 1081–1087. https://doi.org/10.1038/s41563-020-0800-y.

[20] J. Zhou, J. Zhang, Y. Zhi, J. Zhao, T. Zhang, M. Ye, Z. Liu, Partial Regeneration of the Spent SAPO-34 Catalyst in the Methanol-to-Olefins Process via Steam Gasification, Ind. Eng. Chem. Res. 57 (2018) 17338–17347. https://doi.org/10.1021/acs.iecr.8b04181.

[21] L.R. Aramburo, J. Ruiz-Martínez, L. Sommer, B. Arstad, R. Buitrago-Sierra, A. Sepúlveda-Escribano, H.W. Zandbergen, U. Olsbye, F.M.F. de Groot, B.M. Weckhuysen, X-Ray Imaging of SAPO-34 Molecular Sieves at the Nanoscale: Influence of Steaming on the Methanol-to-Hydrocarbons Reaction, Chem. Cat. Chem. 5 (2013) 1386–1394. https://doi.org/10.1002/cctc.201200670.

[22] B. Arstad, A. Lind, J.H. Cavka, K. Thorshaug, D. Akporiaye, D. Wragg, H. Fjellvåg, A. Grønvold, T. Fuglerud, Structural Changes in SAPO-34 Due to Hydrothermal Treatment. A NMR, XRD, and DRIFTS Study, Micropor. Mesopor. Mat. 225 (2016) 421–431. https://doi.org/10.1016/j.micromeso.2016.01.024.

[23] M. Derewinski, M. Briend, M.J. Peltre, P.P. Man, D. Barthomeuf, Changes in the Environment of Silicon and Aluminum in SAPO-37 Zeolite during Acidity Measurements, J. Phys. Chem. 97 (1993) 13730–13735. https://doi.org/10.1021/j100153a049.

[24] A. Buchholz, W. Wang, M. Xu, A. Arnold, M. Hunger, Thermal Stability and Dehydroxylation of Brønsted Acid Sites in Silicoaluminophosphates H-SAPO-11, H-SAPO-18, H-SAPO-31, and H-SAPO-34 Investigated by Multi-Nuclear Solid-State NMR Spectroscopy, Micropor. Mesopor. Mat. 56 (2002) 267–278. https://doi.org/10.1016/S1387-1811(02)00491-2.

[25] Z. Li, J. Martínez-Triguero, J. Yu, A. Corma, Conversion of Methanol to Olefins: Stabilization of Nanosized SAPO-34 by Hydrothermal Treatment, J. Catal. 329 (2015) 379–388. https://doi.org/10.1016/j.jcat.2015.05.025.

[26] T. Fjermestad, S. Svelle, O. Swang, Mechanistic Comparison of the Dealumination in SSZ-13 and the Desilication in SAPO-34, J. Phys. Chem. C. 117 (2013) 13442–13451. https://doi.org/10.1021/jp4028468.

[27] L. Karwacki, E. Stavitski, M.H.F. Kox, J. Kornatowski, B.M. Weckhuysen, Intergrowth Structure of Zeolite Crystals as Determined by Optical and Fluorescence Microscopy of the Template-Removal Process, Angew. Chem. Int. Ed. 46 (2007) 7228–7231. https://doi.org/10.1002/anie.200702012.

[28] L. Marchese, J. Chen, P.A. Wright, J.M. Thomas, Formation of Hydronium Ions at the Brønsted Site in SAPO-34 Catalysts, J. Phys. Chem. 97 (1993) 8109–8112. https://doi.org/10.1021/j100133a001.

[29] J. Chen, P.A. Wright, J.M. Thomas, S. Natarajan, S.M. Bradley, G. Sankar, C.R.A. Catlow, P.L. Gai-Boyes, R.P. Townsend, C.M. Lok, SAPO-18 Catalysts and their Brønsted Acid Sites, 98 (1994) 10216–10224.

[30] M. Castro, Templating Approaches to the Synthesis of New Microporous Materials for Gas Adsorption and Separation, PhD Thesis, St Andrews, 2008.

[31] D.C. Palmer, CrystalDiffract 6.9, Begbrooke, Oxfordshire, UK, 2020

[32] A.C. Larson, R.B. von Dreele, GSAS, General Structure Analysis System, Los Alamos National Laboratory, Los Alamos, NM, 1986

[33] B.H. Toby, EXPGUI. A Graphical User Interface for GSAS, J. Appl. Cryst. 34 (2001) 34, 210-213. https://doi.org/10.1107/S0021889801002242

[34] CrystalClear-SM Expert v2.1, Rigaku Americas, The Woodlands, Texas, USA, and Rigaku Corporation, Tokyo, Japan, 2015.

[35] CrysAlisPro v1.171.38.46., Rigaku Oxford Diffraction, Rigaku Corporation, Oxford, UK, 2015.

[36] G.M. Sheldrick, SHELXT – Integrated Space-Group and Crystal-Structure Determination, 2015, 71, 3-8., Acta Crystallogr., Sect. A. 71 (2015) 3–8.

[37] G.M. Sheldrick, Crystal Structure Refinement with SHELXL, Acta Crystallogr., Sect. C. 71 (2015) 3–8.

[38] A.L. Spek, PLATON SQUEEZE: a Tool for the Calculation of the Disordered Solvent Contribution to the Calculated Structure Factors., Acta Crystallogr. Sect C. 71 (2015) 9–18.

[39] A.L. Spek, Structure Validation in Chemical Crystallography, Acta Crystallogr. Sect D. 65 (2009) 148–155.

[40] CrystalStructure v4.3.0., Rigaku Americas, The Woodlands, Texas, USA, and Rigaku Corporation, Tokyo, Japan., 2018.

[41] A. Buchholz, W. Wang, M. Xu, A. Arnold, M. Hunger, Sequential Steps of Ammoniation of the Microporous Silicoaluminophosphates H-SAPO-34 and H-SAPO-37 Investigated by In Situ CF MAS NMR Spectroscopy, J. Phys. Chem. B. 108 (2004) 3107–3113. https://doi.org/10.1021/jp030249d.

[42] K. De Wispelaere, C.S. Wondergem, B. Ensing, K. Hemelsoet, E.J. Meijer, B.M. Weckhuysen, V. Van Speybroeck, J. Ruiz-Martínez, Insight into the Effect of Water on the Methanol-to-Olefins Conversion in H-SAPO-34 from Molecular Simulations and in Situ Microspectroscopy, ACS Catal. 6 (2016) 1991–2002. https://doi.org/10.1021/acscatal.5b02139.

[43] G. Cinque, M. Frogley, K. Wehbe, J. Filik, J. Pijanka, Multimode InfraRed Imaging and Microspectroscopy (MIRIAM) Beamline at Diamond, Synchro. Radiat. News. 24 (2011) 24–33. https://doi.org/10.1080/08940886.2011.618093.

[44] G. Liu, P. Tian, Y. Zhang, J. Li, L. Xu, S. Meng, Z. Liu, Synthesis of SAPO-34 templated by diethylamine: Crystallization Process and Si Distribution in the Crystals, Micropor. Mesopor. Mat. 114 (2008) 416–423. https://doi.org/10.1016/j.micromeso.2008.01.030.

[45] M. Briend, R. Vomscheid, M.J. Peltre, P.P. Man, D. Barthomeuf, Influence of the Choice of the Template on the Short- and Long-Term Stability of SAPO-34 Zeolite, J. Phys. Chem. 99 (1995) 8270–8276. https://doi.org/10.1021/j100020a060.

[46] F. Wei, Y. Jin, Y. Cheng, Chapter 8. Methanol to Lower Olefins and Methanol to Propylene, in: Multiphase Reactor Engineering for Clean and Low-Carbon Energy Applications, John Wiley & Sons, Inc., Hoboken, New Jersey, 2017: pp. 271–294.

[47] B. Zibrowius, E. Löffler, M. Hunger, Multinuclear MAS NMR and IR Spectroscopic Study of Silicon Incorporation into SAPO-5, SAPO-31, and SAPO-34 Molecular Sieves, Zeolites. 12 (1992) 167–174. https://doi.org/10.1016/0144-2449(92)90079-5.

[48] I. Halasz, B. Moden, A. Petushkov, J.-J. Liang, M. Agarwal, Delicate Distinction between OH Groups on Proton-Exchanged H-Chabazite and H-SAPO-34 Molecular Sieves, J. Phys. Chem. C. 119 (2015) 24046–24055. https://doi.org/10.1021/acs.jpcc.5b09247.

[49] S. Bordiga, L. Regli, D. Cocina, C. Lamberti, M. Bjørgen, K.P. Lillerud, Assessing the Acidity of High Silica Chabazite H−SSZ-13 by FTIR Using CO as Molecular Probe: Comparison with H−SAPO-34, J. Phys. Chem. B. 109 (2005) 2779–2784. https://doi.org/10.1021/jp045498w.

[50] E. Fois, A. Gamba, G. Tabacchi, Structure and Dynamics of a Bronsted Acid Site in a Zeolite: An ab initio Study of Hydrogen Sodalite, J. Phys. Chem. B 102 (1998) 3974-3979. https://doi.org/10.1021/jp9808274

[51] D. Freude. J. Klinowski, H. Hamdam, Solid-State NMR Studies of the Geometry of Brønsted Acid Sites in Zeolitic Catalysts, Chem. Phys. Lett. 149 (1988) 355-362. https://doi.org/10.1016/0009-2614(88)85107-8

[52] A. Vjunov, M. Wang, N. Govind, T. Huthwelker, H. Shi, D. Mei, J. L. Fulton, J. Lercher, Tracking the Chemical Transformations at the Bronsted Acid Site upon Water-Induced Deprotonation in a Zeolite Pore, Chem. Mater. 29 (2017) 9030-9042. https://doi.org/10.1021/acs.chemmater.7b02133

[53] J.H. Kang, F.H. Alshafei, S.I. Zones, M.E. Davis, Cage-Defining Ring: A Molecular Sieve Structural Indicator for Light Olefin Product Distribution from the Methanol-to-Olefins Reaction, ACS Catal. 9 (2019) 6012-6019. https://doi.org/10.1021/acscatal.9b00746

[54] D. Chen, K. Moljord, T. Fuglerud, A. Holmen, The Effect of Crystal Size of SAPO-34 on the Selectivity and Deactivation of the MTO Reaction, Micropor. Mesopor. Mater. 29 (1999) 191-203. https://doi.org/10.1016/S1387-1811(98)00331-X

[55] X. Yuan, H. Li, M. Ye, Z. Liu, Comparative Study of MTO Kinetics over SAPO-34 Catalyst in Fixed and Fluidized Bed Reactors, Chem. Eng. J. 329 (2017) 35-44. http://dx.doi.org/10.1016/j.cej.2017.04.041

[56] D. Mores, E. Stavitski, M.H.F. Kox, J. Kornatowski, U. Olsbye, B.M. Weckhuysen, Space- and Time-Resolved In-situ Spectroscopy on the Coke Formation in Molecular Sieves: Methanol-to-

Olefin Conversion over H-ZSM-5 and H-SAPO-34, Chem. Eur. J. 14 (2008) 11320–11327. https://doi.org/10.1002/chem.200801293.

[57] C. Coelho, T. Azaïs, L. Bonhomme-Coury, G. Laurent, C. Bonhomme, Efficiency of the Refocused ^{31}P–^{29}Si MAS-J-INEPT NMR Experiment for the Characterization of Silicophosphate Crystalline Phases and Amorphous Gels, Inorg. Chem. 46 (2007) 1379–1387. https://doi.org/10.1021/ic061964f.

[58] I.B. Minova, S.K. Matam, A. Greenaway, C.R.A. Catlow, M.D. Frogley, G. Cinque, P.A. Wright, R.F. Howe, Elementary Steps in the Formation of Hydrocarbons from Surface Methoxy Groups in HZSM-5 Seen by Synchrotron Infrared Microspectroscopy, ACS Catal. 9 (2019) 6564–6570. https://doi.org/10.1021/acscatal.9b01820.

[59] I.B. Minova, S.K. Matam, A. Greenaway, C.R.A. Catlow, M.D. Frogley, G. Cinque, P.A. Wright, R.F. Howe, Effects of Crystal size on Methanol to Hydrocarbon Conversion over Single Crystals of ZSM-5 Studied by Synchrotron Infrared Microspectroscopy, Phys. Chem. Chem. Phys. 22 (2020) 18849–18859. https://doi.org/10.1039/D0CP00704H.

[60] I.B. Minova, S.K. Matam, C.R.A. Catlow, M.D. Frogley, G. Cinque, M. Buehl, P.A. Wright, R.F. Howe, Formation and Reactivity of Methoxy Groups in SAPO-34, (2021) (in preparation).

[61] Q. Qian, J. Ruiz-Martínez, M. Mokhtar, A.M. Asiri, S.A. Al-Thabaiti, S.N. Basahel, B.M. Weckhuysen, Single-Particle Spectroscopy of Alcohol-to-Olefins over SAPO-34 at Different Reaction Stages: Crystal Accessibility and Hydrocarbons Reactivity, Chem. Cat. Chem. 6 (2014) 772–783. https://doi.org/10.1002/cctc.201300962.

[62] I.B. Minova, N.S. Barrow, A. Sauerwein, A.B. Naden, D.B. Cordes, A.M.Z. Slawin, S. Schuyten, P.A. Wright, 2020, Silicon Redistribution, Acid Site Loss and the Formation of a Core-Shell Texture upon Steaming SAPO-34 and their Impact on Catalytic Performance in the MTO Reaction (dataset). University of St Andrews Research Portal. https://doi.org/10.17630/09ddc03e-f121-4e79-9b55-674f64d9c8c4